Photoelectrochemical and Physical Properties of Ti Oxide Films made by Sputtering: *Towards a New Dye-Sensitized Nanocrystalline Solar Cell*

LICENTIATE THESIS

BY

MÓNICA GÓMEZ

UPPSALA UNIVERSITY
DEPARTMENT OF MATERIALS SCIENCE
1999

Photoelectrochemical and Physical Properties of Ti Oxide Films made by Sputtering: *Towards a New Dye-Sensitized Nanocrystalline Solar Cell*

LICENTIATE THESIS

BY

MÓNICA GÓMEZ

Para mi amor, aquí una parte de nuestro esfuerzo, siempre tuya...
Mónica

UPPSALA UNIVERSITY
DEPARTMENT OF MATERIALS SCIENCE
1999

PHOTOELECTROCHEMICAL AND PHYSICAL PROPERTIES OF Ti OXIDE FILMS MADE BY SPUTTERING: *TOWARDS A NEW DYE-SENSITIZED NANOCRYSTALLINE SOLAR CELL*

Contents

1. INTRODUCTION

This chapter gives a general view of the current trends in the field of dye-sensitized solar cells. The basic system for this type of cell will be introduced. The aim of this thesis is also explained. Section 1.1 gives an overview of the field. In order to understand how the high internal surface area can improve the efficiency of the dye-sensitized solar cell, some facts concerning how it works are given in section 1.2. Finally in section 1.3. the scope of the present work is described.

1.1. Overview

The utilization of solar energy has attracted a lot of attention since the energy crisis of the 70's. This energy source is of particular interest because the sun provides free, non-exhaustible, non-polluting energy. And it is known from consumption trends that fossil fuel -coal, oil and natural gas- will not be sufficient for another hundred years. Even though there are other non-fuel resources such as hydropower, geothermal energy, wind energy, and wave energy, etc, solar energy is believed to be the most important. Solar cells in particular are considered a major candidate for obtaining energy from the sun, because of their ability to convert sunlight directly to electricity with high conversion efficiency and their ecological compatibility [1,2]. However, at present, economics sets limitations for the large scale-use of solar cells. In spite of this its large scale–use is feasible in some applications such as satellites, space vehicles, and some small-scale terrestrial applications e.g. rural electrification [3] and telecommunication stations. On the other hand, photovoltaic cells today have huge applications for low power devices such as watches, calculators and small electronic instruments. So, the major goal in solar cell development for energy research is to prepare them in an inexpensive way with high conversion efficiency so that they are attractive for large-scale industrial production.

Solar cell technology based on a photoelectrochemical process was recognized as an important solar energy device around 1970 [4] and after that many studies were performed for the mechanistic interpretation of the role of electrons and holes in electrode-electrolyte interfaces [5]. One important approach discussed the possibility of sensitizing the electrodes with dyes [6] which are absorbed on the surface of the electrodes. But the quantum efficiency was limited by the fact that only monolayers of dyes were active for electron transfer to the semiconductor in the excited state, so the absorption of light was only in the order of 1-2%.

In 1980, notable progress was made by Matsumura et al. who prepared the first dye-sensitized large internal area electrode [7]. This led to a breakthrough in further development and nowadays the solar conversion efficiency of a dye-sensitized electrode is about 10% [8,9] which is competitive with solid state technology. This porous cell consists of small particles which form a porous network of nanometer sized semiconductor crystals deposited on a conducting substrate. The stability of this type of solar cell is not yet fully understood and currently a lot of work is being carried out to develop this system and understand it in more detail [10-14].

1.2. Dye-sensitized solar cell

Dye-sensitized solar cells consist of a sensitized nanostructured semiconductor electrode, an electrolyte and a counter electrode. The dye is adsorbed throughout the entire surface of the film, and the electrolyte penetrates the nanostructured film all the way to the back contact.

Figure 1.1 displays an energy diagram showing the electronic structure in dye-sensitized nanostructured solar cells. The n-type semiconductor, such as titanium oxide, is considered in particular, because so far this is the material most studied for this purpose.

When the light is absorbed by the system, (1) the electrons are excited from VB to CB in the semiconductor, generating electron-hole pairs, and (2) the excitation of the dye molecules produces the injection of electrons into the semiconductor. At the counter electrode, electrons are transferred to redox species in the electrolyte. The redox molecules can diffuse to the oxidized dye molecules and return the electrons, and the cycle is completed.

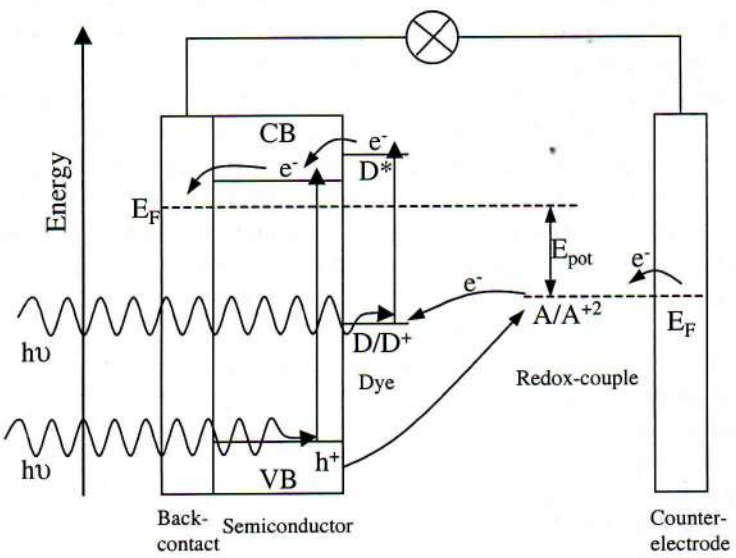

Figure 1.1 *Energy scheme for dye-sensitized nanostructured solar cell. By absorption of light, the dye passes from the electronic ground state to the excited state. It then injects an excited electron into the conduction band of the semiconductor (titanium oxide) and thus becomes oxidized. The other possibility is the formation of the electron-hole pair due to the electron excitation from the VB to the CB. Then the electrolyte is reduced at the counter electrode and the cycle is completed.*

1.3. The focus of this work

The present work focuses on the preparation of sputter-deposited titanium oxide films for dye-sensitized solar cell purposes, since sputtering as a thin film preparation technique is of particular significance owing to its well documented upscaling capability and industrial viability [15,16].

Nanostructured electrodes have the advantage of having high surface areas formed by nanoparticle networks, which allows not only the high adsorption of the dye in the surface of the semiconductor, but also the penetration of the electrolyte in the interconnected pores. So far titanium oxide, which is prepared by chemical techniques from alcoxides or is commercially available as a powder, is the porous material most studied [8-14]. In spite of the highly significant progress made for electrical energy conversion efficiency of dye-sensitized photoelectrochemical solar cells, this type of system still faces many problems because different parameters influence the efficiency of the cell, *e.g.* surface treatment, size of the pores, crystal dimensions, film thickness, dye, electrolyte and semiconductor. Some of these parameters are difficult to control by the normal techniques mentioned above which are used for the preparation of the electrodes. On the other hand, sputtering techniques show proved reproducibility and high upscaling capabilities.

One of the purposes of this work is to produce durable dye-sensitized solar cells with high efficiency. To achieve this goal, the DC-magnetron sputtering technique using two types of substrates with completely different surface roughness was chosen. Besides the technical aim, which is the high impact for industrial proposes, the goal was also to perform basic physical-chemistry studies in order to contribute to a further and more complete understanding of dye-sensitized solar cells. That is why some techniques in order to determine the structure of the obtained material, the morphology of the surface and the presence of the dye in the electrode have been used.

2. THE SEMICONDUCTOR-ELECTROLYTE INTERFACE

When a semiconductor is brought into contact with an electrolyte containing a redox couple many processes are developed. These processes are the basis of photoelectrochemistry. The present section reviews some basic semiconductor concepts and some fundamental electrochemistry, as well as the fundamental principles of the semiconductor-electrolyte interface with respect to light to electrical energy conversion. Finally, the fundamentals of dye-sensitized electrodes will be presented.

2.1 The semiconductor

A solid material is a three-dimensional array of many atoms. To understand the properties and structure of the solid systems, a quantum mechanical treatment is required. Quantum theory says that the interaction between two atomic orbitals is represented by the sum of two wavefunctions which characterize discrete levels of energy for an electron in an atom, and that the interaction between energy states depends on orbital penetration, shielding of the nuclear charge and the differences in energy.

If several atoms are brought together to build a solid, i.e. crystal lattice, the electron levels are split, forming new energy levels with a separation that decreases with increasing number of atoms. These spacings can be so small that they can be considered as a continuous band.

Some energy bands will be completely filled with electrons and others will be empty or partially filled. Three types of solids are distinguished by the temperature dependence of their electrical conductivity. A metal has partially filled or overlapping bands. This gives a highly conducting material since the electrons can move freely between empty and filled energy states. In a metal conductor, its conductivity decreases as the temperature is raised. The second type is an insulator in which the band gap i.e., the difference between the highest occupied level (E_v) and the lowest unoccupied level (E_c), generally is above 4 eV, so thermal excitation will lead a non-conducting material. The third type of solid is a semiconductor, whose band gap is of such a size that thermal excitation can produce observable conductivity at temperatures below its melting point. A semiconductor has a conductivity that increases as the temperature is raised.

2.1.1. The Fermi level

The electrons of a solid crystal at thermal equilibrium obey Fermi-Dirac statistics. The Fermi-Dirac function, $f(E)$, describes the distributions of the electrons within the allowed energy levels

$$f(E) = \frac{1}{e^{(E-E_F)/kT} + 1}, \qquad (2.1)$$

where E is the energy of the particular energy level and E_F is the Fermi level where the probability of a level being occupied by an electron is ½. In a perfect intrinsic semiconductor, the Fermi level lies in the middle of the band gap at zero Kelvin, Fig. 2.1a. However, that position depends on the electronic structure of the solid and the temperature, so when impurity atoms are introduced, the Fermi level must adjust itself to preserve charge neutrality [21,22]. In addition, the Fermi level can be affected by illumination and applied potential. The Fermi level has a fundamental importance as the electrochemical potential for electrons in the solid.

2.1.2. Impurity levels in the semiconductor

If a few ppm of a specific impurity are introduced into the lattice of the solid, the conductivity of the material can increase dramatically. Impurities that contribute to the carrier density of a semiconductor are called *donors* (n-type) if they supply additional electrons to the conduction band, and *acceptors* (p-type) if they supply additional holes to the valence band.

A well-known example is the influence of As with its five valance electrons in Si which is an element with four balance electrons. The fifth electron around As will be accommodated in an energy level (D_E) only about 0.05 eV below the conduction band of Si and is readily thermally excited from this donor level to the conduction band. Consequently, the Fermi level moves upwards, lying close to the conduction band (Fig. 2.1b). On the other hand, if trivalent atoms such as Al are added to the Si lattice, acceptor energy levels are created just above (~0.045 eV) the valence band of Si. Electrons can be thermally excited from the valence band to the acceptor levels. The remaining holes are then available for conduction. In this case the Fermi level moves downwards and will lie close to the valence band (Fig. 2.1c) [23-25].

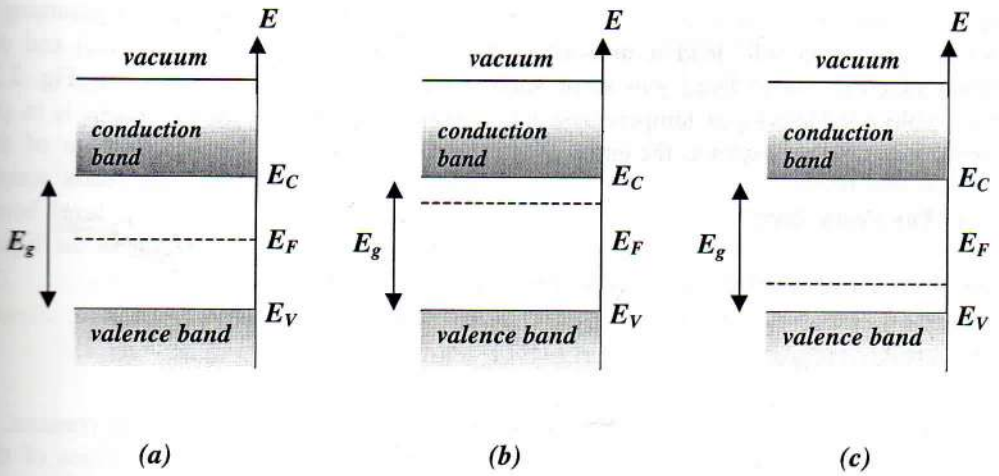

Figure 2.1. *Schematic picture of energy diagrams (a) intrinsic, (b) n-doped, (c) p-doped semiconductors.*

2.1.3. Ti oxide

Titanium oxide is a semiconductor that holds much promise for photoelectrochemical applications related to energy conversion [6]. The material is of great interest for dye-sensitized solar cells [8], for the photocatalytic destruction of organic pollutants in wastewater [18-20] and for electrochromic devices [26]. It is also useful for the industrial production of some materials such as paints, toothpaste and sun block. Because it is hard and chemically resistant, it is also used as a protective coating material.

Titanium oxide exists in three different crystal structures: rutile, anatase and brookite. Anatase and rutile are the most common and they are both tetragonal phases with similar densities (anatase 3.89 g/cm^3 and rutile 4.26 g/cm^3). They are transparent in the visible and the near infrared ranges, and have band gaps of 3.0 eV (rutile) and 3.2 eV (anatase). Rutile is thermodynamically more stable under normal conditions and is generally obtained at temperatures above 700°C at atmospheric pressure.

Defect doping of large crystals is due to slight oxygen deficiency, which leaves electrons in the conduction band, yielding an n-type semiconductor.

2.2 The electrolyte

The electrolyte has an important role in a dye-sensitized solar cell because it is responsible for many steps in the function of that solar cell. The electrolyte consists of a solvent with dissolved redox couples.

The electrolyte has empty and occupied energy levels in the dissolved redox system, which corresponds to the conduction and valence bands in the solid semiconductor, respectively. The distribution of the energy levels associated with the redox couple will define the tendency to donate or accept electrons when the redox molecules approach the solid electrode. The energy states of the redox couples are distributed over a certain range, due to fluctuation in the solvation shell surrounding the redox molecules. So, assuming a harmonic oscillation of the solvation shell, the density of occupied states (D_{red}) and the density of empty states (D_{ox}) can be described by Gaussian types of functions (Fig. 2.2) [17]. Thus the energy position of the level of the dissolved ox- and red- forms is in the maximum of the Gaussian function. The intersection point of the distribution of the oxidized and reduced species represents the solution redox potential of the redox couple $E_{red/ox}$, and since this point represents the stage where the probability of a level being occupied by an electron is ½, $qE_{red/ox}$ can be considered as the Fermi level in the liquid phase. The potential $E_{red/ox}$ can be calculated using the Nernst equation.

$$E_{red/ox} = E^{o}_{red/ox} + \frac{RT}{nF} \ln \frac{\{ox\}}{\{red\}}, \qquad (2.2)$$

where n is the number of electrons transferred in the redox reaction, R is the gas constant, T is the temperature, F is Faraday's constant and $\{ox\}$ and $\{red\}$ are the activities of the oxidized and reduced species of the redox molecule.

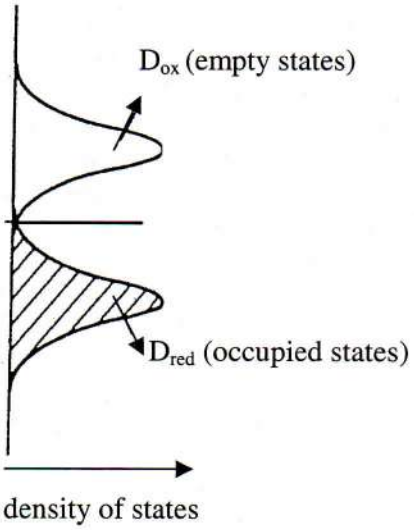

Figure 2.2. *Distribution function of the redox system.*

In electrochemistry the redox potential of the normal hydrogen electrode is defined as zero, while for a semiconductor the vacuum level is the zero in an absolute scale. The relation between these two energy scales is given by [27,28].

$$E_F = -4.6 - qE_{red/ox}\ (eV), \qquad (2.3)$$

Where q is the elementary charge (Fig. 2.3).

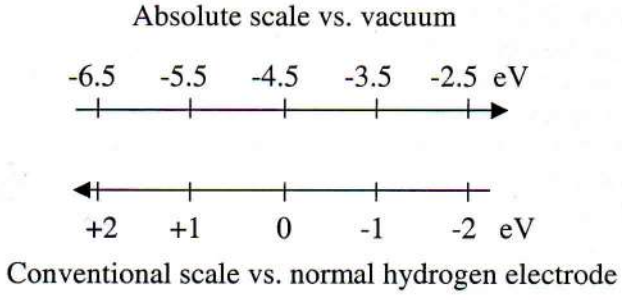

Figure 2.3. *Absolute energy scale used in semiconductors and the electrochemical scale with the NHE.*

2.3 Semiconductor in contact with an electrolyte

When a semiconductor and an electrolyte with different electrochemical potentials are brought into contact, the equilibrium is attained by exchanging charges until the chemical potential in both phases becomes equal. Specifically, let us consider as an example a system containing an n-type semiconductor and an electrolyte with one redox couple, where the Fermi level in the solid electrode initially is at higher energy that the electrochemical potential of the electrolyte (Fig. 2.4a). In this system, to obtain the equilibrium, electrons in the semiconductor will be transferred to the electrolyte until the Fermi level is adjusted to the chemical potential (Fig. 2.4b). This process produces a positive charge in the semiconductor and a built-in electric field lending to the bend of the bands in a region called the depletion layer. This space charge region is typically in the range of a few nanometers, to micrometers, depending on the initial difference in electrochemical potential of the two phases, the dielectric constant and the charge carrier density. On the other hand, a negative counter charge, called the Helmholtz layer, develops in the electrolyte, extending generally atomic distances from the surface. In the absence of space charge, the bands are flat from the bulk to the surface of the semiconductor and the corresponding redox potential is called the "flat band potential" (Figure 2.4c)) [27,28]. The semiconductor-electrolyte interface has many features similar to the Schottky-type barrier (metal-semiconductor interface) where we can consider that the electrolyte behaves like a metal.

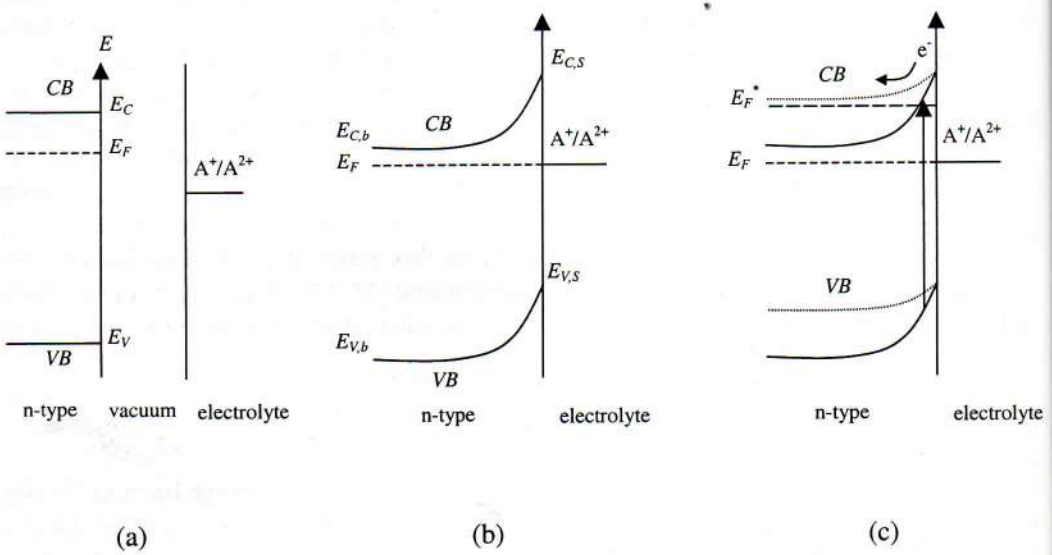

Figure 2.4. *Energy level diagrams for an n-type semiconductor and a redox couple in the electrolyte. (a) No contact between the semiconductor (in vacuum) and the electrolyte. (b) Semiconductor in equilibrium with an electrolyte. (c) Flat band position for the semiconductor* [27].

2.3.1. Illumination and photoeffects

Light-induced charge separation and subsequent chemical reactions at the semiconductor electrolyte interface are the basis of photoelectrochemistry. This can be explained by considering again as an example a system consisting of an n-type semiconductor in contact with an electrolyte, illuminated by light of energy greater than or equal to the band gap. The absorbed photons will generate the electron-hole pairs, which will be separated by the built-in electric field, so the holes will be driven to the surface while the electrons can be transported away into the bulk of the semiconductor to do useful work. A restriction for the electrons and holes to be transferred to redox molecules in the electrolyte is that the edges of the valence and conduction bands straddle the energy of the redox couple in the electrolyte. Under open-circuit conditions the excited electrons will accumulate in the conduction band and the Fermi level will rise above the redox potential of the solution, so a photopotential will be created. If the illumination continues, flat band conditions will be reached under certain ideal conditions and the maximum photovoltage can be obtained [28]. Normally we work under non-ideal conditions and the efficiency of the charge separation process will be affected by surface states, traps and recombination processes.

2.4 Dye sensitization

The energy conversion of a solar cell depends on the spectral response of the cell, so if the absorption edge of the semiconductor is just below the energy of the maximum solar emission, a rather high efficiency can be obtained. The optimal values of the band gaps are in the range of 1.1 - 2.1 eV. Silicon is the most efficient material for a solid state device, but is not suitable for an electrochemical cell, due to its high reactivity with most solvents. One of the semiconductors which is known to be stable against such an attack is titanium oxide. However, this material was excluded [17] from practical applications because its large band gap allows only the absorption of light in the UV range. But now it is well known that one way to improve the efficiency of this material is by sensitization with molecules (organic dyes or small semiconductor clusters) [29-33] which can absorb the light in the visible range. In this section a review of the basis of dye sensitization and the dye used in this work will be presented.

2.4.1. The basis of dye-sensitization

Dye-sensitized electrodes are sensitive to wavelengths in the visible range because the dye increases the spectral response of the system. During illumination a dye molecule absorbs light and the excited molecule transfers charge to the semiconductor. The regeneration of the dye is possible by the oxidation of the redox couple in the electrolyte, which should have a more negative redox potential than the ground state of the dye, Fig.2.5. Some of the aspects to be considered to make the sensitization process efficient are the relative position between the molecular orbitals in the dye and the energy bands in the semiconductor; a good orbital overlap is also required to facilitate the electron transfer.

It has been found that very porous electrodes give high light absorption [34] and high conversion efficiency.

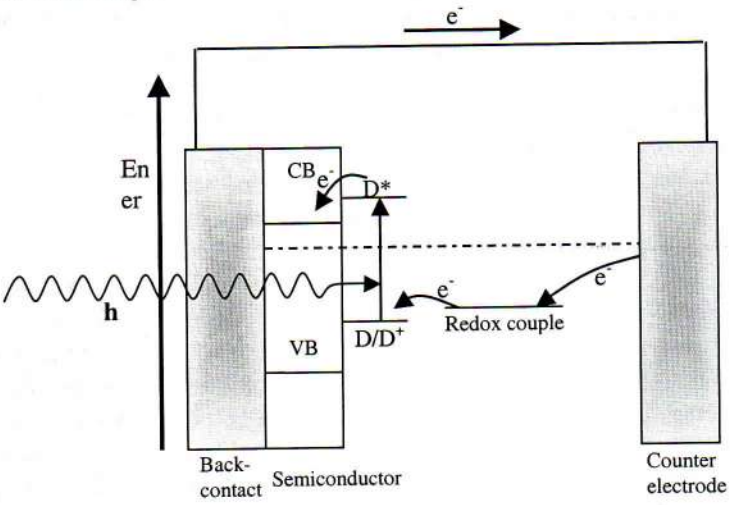

Figure 2.5. *Energy diagram for a dye-sensitized electrode under illumination* [35].

2.4.2. The dye

The dye used in this work is cis-dithiocyanato-bis(2,2'-bipyridyl-4,4'dicarboxylate)-ruthenium (II), see Fig. 2.6., which has a broad absorption spectrum and gives very high injection yield on titanium oxide for nanostrutured electrodes [33]. Many ruthenium complexes have been studied for dye sensitization purposes, but so far the molecule mentioned above gives the best performance for dye-sensitized solar cells.

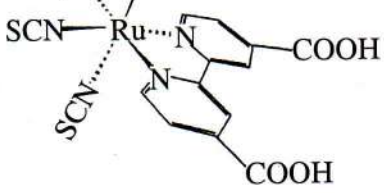

Figure 2.6. *Chemical structure of the cis-dithiocyanato-bis(2,2'-bipyridyl-4,4'-dicarboxylate)-ruthenium (II), the dye used in this work.*

3. EXPERIMENTAL TECHNIQUES

This section describes the experimental techniques that have been used for sample preparation and characterization of the films. It is divided into three parts:

1. preparation of the films
2. physical characterization
3. electrochemical and photoelectrochemical characterization.

3.1 Sample preparation

3.1.1 Sputtering: general discussion

Sputtering is one of the most commonly used methods for the deposition of thin films [36]. It consists of the ejection of material from the surface of a solid through the collision of energetic particles such as ions, neutrons, electrons or photons. The material to be covered is placed as a target (cathode), in the form of a plate and is connected to a power supply. Sputtering techniques range from simple DC glow discharge sputtering which is limited to the sputtering of conductive targets, to RF sputtering where any target, regardless of its conductivity, can be sputtered.

Sputtering is related to momentum transfer from energy particles to the surface atoms of the target [37]. Sputtering has been described as an "atomic pool" where the ion (cue ball) breaks up the close-packed rack of atoms (billiard balls), scattering some backward (toward the player). Figure 3.1 gives a pictorial description of the sputtering as a sort of "atomic billiard game". Sputtering theory uses the assumption of elastic binary collisions, even though atoms of solids are bound to each other by a complex interatomic potential.

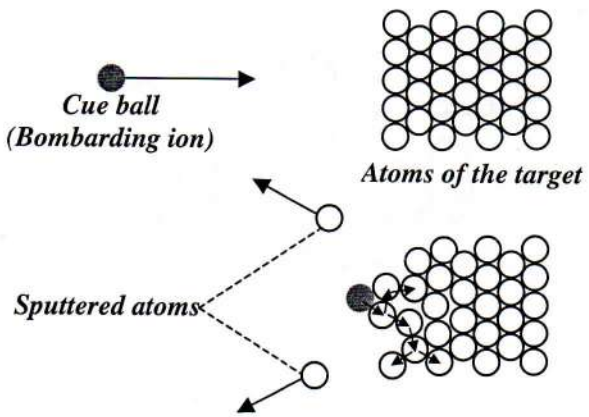

Figure 3.1. *Billiard ball model of sputtering* [38].

The most fundamental parameter characterizing sputtering is the sputter yield Y which is the mean number of atoms or molecules ejected from a target surface per incident ion. The sputter yield has a clear dependence on the atomic number of the ion and its angle of incidence.

Sputtering is always carried out in a gas atmosphere with sputtering gas pressure of a few mTorr. This may lead to the incorporation of the sputtering gas in the film.

3.1.2. Direct current glow discharge sputtering

DC glow discharge sputtering is one of the simplest techniques. The limitation is that non-conductive targets cannot be sputtered. In this mode the target is connected to a DC power supply capable of supplying several kilovolts. The substrates can be electrically grounded, biased or left floating. Applying a negative bias voltage on the substrate, ions from the sputtering discharge are accelerated towards the growing film surface. These ions result in the resputtering of deposited atoms, which enhances the surface mobility of the adsorbed atoms and results in increased film density.

As the applied target voltage increases, more and more charge carriers are created due to secondary electrons that are emitted from the target or from impact, so the current increases and the "Townsend discharge" [39] is obtained. This is the beginning of an avalanche that leads to a steady state where the number of electrons and ions produced becomes the same and the plasma self-sustaining. This is the "normal glow" state. Next, the glow becomes increasingly visible, accompanied by a sharp rise in the current and a drop in the voltage; this is the "abnormal glow" state.

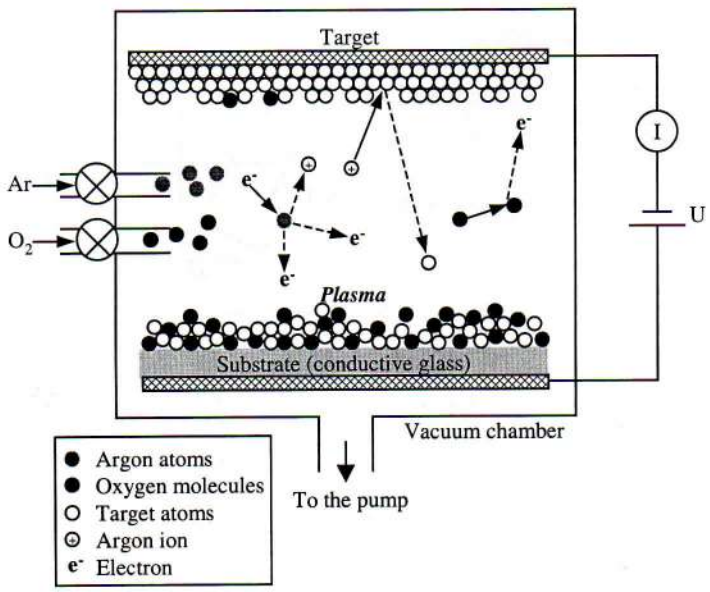

Figure 3.2. *Schematic dc-glow discharge sputtering system containing reactive gas* [40].

3.1.3. Magnetron enhanced DC sputtering

The goal of using a magnetic field in a sputtering system is to increase the ionization by making more efficient use of the electrons.

When a magnetic field of strength B is superimposed on the electric field E between the target and the substrate, the electrons within this dual field environment experience the Lorentz force:

$$F = \frac{mdv}{dt} = -q(E + v \times B), \qquad (3.1)$$

where q, m and v are the electron charge, the mass and the velocity, respectively. If an electron is launched from the cathode with velocity v at angle θ with respect to B, it experiences a force $qvBsin\theta$ in a direction perpendicular to B. The electron now orbits in a circular motion with a radius r that is determined by a balance of centrifugal $(m(vsin\theta)^2/r)$ and Lorentz forces, i.e., $r=mvsin\theta/qB$. The electron motion is helical, it spirals down the axis of the discharge with constant velocity $vcos\theta$. Therefore, the magnetic field enhances ionization in two ways. First, it reduces the velocity of the electrons towards the walls to zero. Second, the longer helical orbit increases the total path traveled by an electron, thus enabling it to cause more ionization and excitation [41].

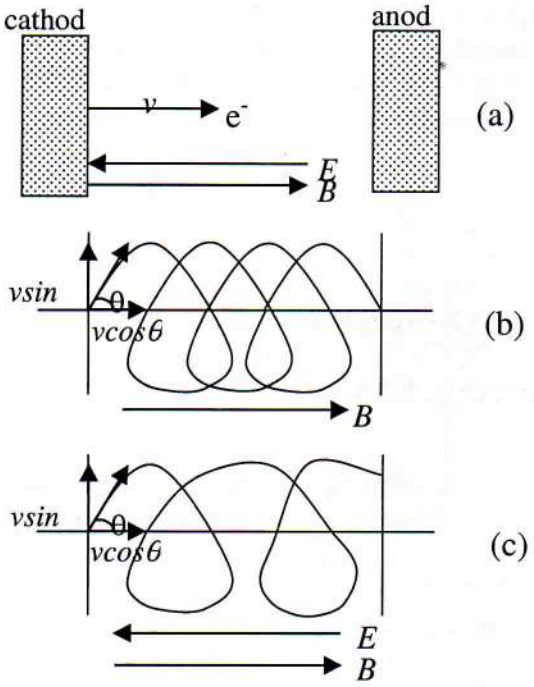

Figure 3.3. *Effect of E and B on electron motion. (a) Linear electron trajectory when E // B ($\theta = 0$); (b) helical orbital of constant pitch when $B \neq 0$, $E = 0$, ($\theta \neq 0$); (c) helical orbital of variable pitch when E // B ($\theta \neq 0$) [41].*

3.1.4. Reactive sputtering

In reactive sputtering, thin films are deposited on substrates by sputtering from metallic targets in the presence of one or several reactive gases which are usually mixed with the inert working gas (invariably Ar). In reactive sputtering, the sputter gas contains a reactive gas such as oxygen, nitrogen, methane, H_2S, etc., This reactive gas can react with the target, with the sputter atoms or the grown film, producing oxides, nitrates, carbides, sulphites, etc. When the reactive gas is increased, reactions on the target surface will occur until the target becomes poisoned due to the compound covering its surface. Then the compound will be sputtered instead of the pure metal, with a low rate of deposition due to a reduced Y.

3.1.5. Sputter system used in this work

Titanium oxide films were deposited using reactive DC magnetron sputtering in a system based on Balzers UTT 400 vacuum chamber [42]. After evacuation to ~10^{-7} Torr by turbo molecular pumping, sputtering took place in an atmosphere of Ar (99.998%) mixed with O_2 (99.998%). The O_2/Ar gas flow ratio was kept constant at a value Γ during the film deposition, and the sputtering took place in a total gas pressure of ~12 mTorr. The system was equipped with a multi-target system with up to four planar dc magnetron sputter sources. The targets were 5-cm-diameter plates of titanium (99.9%) positioned 13 cm from a substrate holder and tilted 35° with respect to the horizontal plane. The polarity of each magnet was N-S-N. The substrate temperature τ_s was controlled by a resistive heater, and film uniformity was assured by rotating the substrate.

3.2. Physical characterization

3.2.1. Thickness measurements

It is of crucial importance to have an adequate technique for measuring the film thickness because many of the properties of a thin film are thickness dependent. In this work we employed a Tencor alpha-step 200 surface profilometry instrument with a maximum resolution of 5 Å. The surface profile required for thickness determination was obtained by partially masking the sample with a very thin piece of glass sheet in order to obtain a step. A diamond stylus with a radius of 12.5 μm was scanned over the step. The standard scan length was 2,000 μm.

3.2.2. X-ray diffraction

X-ray diffraction is a powerful technique that is used to analyze crystalline materials. Each atom exposed to a beam of X rays is the source of a coherent scattered wave which will interfere in a constructive or destructive way with waves emitted from neighboring atoms. The method embodies a study of a spatial distribution of the total diffracted wave. Thus under ideal conditions, a perfect crystal and an incident beam composed of perfectly parallel

and strictly monochromatic radiation will give a sharp peak in the intensity of the scattered radiation. The path difference between two rays, which interfered constructively, is just $2dsin\theta$, where θ is the angle of incidence and d is the interplanar distance. This leads to the Bragg formulation

$$2dsin\theta = n\lambda, \tag{3.2}$$

where λ is the wavelength of the x ray and n is the order of the reflection.

Ideal conditions never actually exist, so we must determine the effect on diffraction of various kinds of departure from the ideal. We find that a very small crystal (less than about 0.1 μm causes broadening (a small angular divergence) of the diffracted beam. An exact treatment of the problem gives

$$t = \frac{0.9\lambda}{B\cos\theta}, \tag{3.3}$$

which is known as the Scherrer formula and it is used to estimated the particle size of a very small crystal t, by measuring the broadening of the diffraction line B, at half its maximum intensity in radians.

X-ray diffraction (XRD) was carried out by a Siemens D5000 diffractometer with a Cu anode, using either a grazing incidence unit suitable for thin films or a conventional θ-2θ set up. Data from standards for TiO_2 were used to identify the diffraction peaks [43] and Scherrer´s formula [44] was used to estimate the mean grain size.

3.2.3. Atomic force microscopy

Atomic force microscopy (AFM) is only one of the numerous methods of scanning tunneling microscopy (STM) which have been invented in parallel with the development of the STM technique itself [45,46]. All these techniques have in common a tip and a sample surface that are scanned with respect to each other by means of a piezoelectric scanner coupled with electric feedback techniques. In addition, all these techniques have the characteristic that their resolution is not determined by any wavelength that is used for the interaction as in conventional microscopy, but rather by the size of the interacting probe that hovers over the sample surface to scan the image [47].

Figure 3.4 displays the experimental set-up of an AFM. The sample is placed over an XYZ piezoelectric crystal. The cantilever with the tip scans the surface (XY) while a laser beam is reflected on the reverse of the cantilever to a position-sensitive detector connected to a feedback system regulating the high (Z) with the piezoelectric crystal, thereby keeping the atomic force constant. The coordinates for every position are recorded in a computer and the topography can by plotted on a screen. From AFM images, it is possible to obtain information about the grain size and roughness.

The films were characterized using the atomic force microscope, Nanoscope II, an instrument with an etched silicon cantilever which had a tip radius of 10 nm.

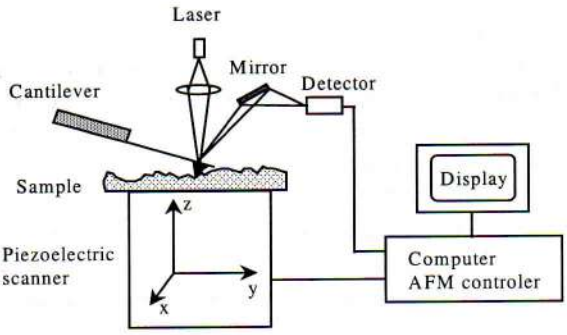

Figure 3.4. *Schematic diagram of an atomic force microscope (AFM)*

3.2.4. Scanning electron microscopy

The principle of the scanning electron microscope (SEM) is shown in Fig. 3.5. Electrons from a thermionic or field-emission cathode are accelerated by a voltage of 1-50 kV between cathode and anode. Then the beam is condensed and collimated by pole-pieces (magnetic lens) until it dissipates its energy in the sample. The spectrum energy of the electrons emitted consists of secondary electrons (SE), backscattering electrons (BSE) and Auger electrons. The SE and BSE carry information about the sample topography. One important advantage of SEM is the wide variety of electron-specimen interaction that can be used to form an image and to furnish qualitative and quantitative information.

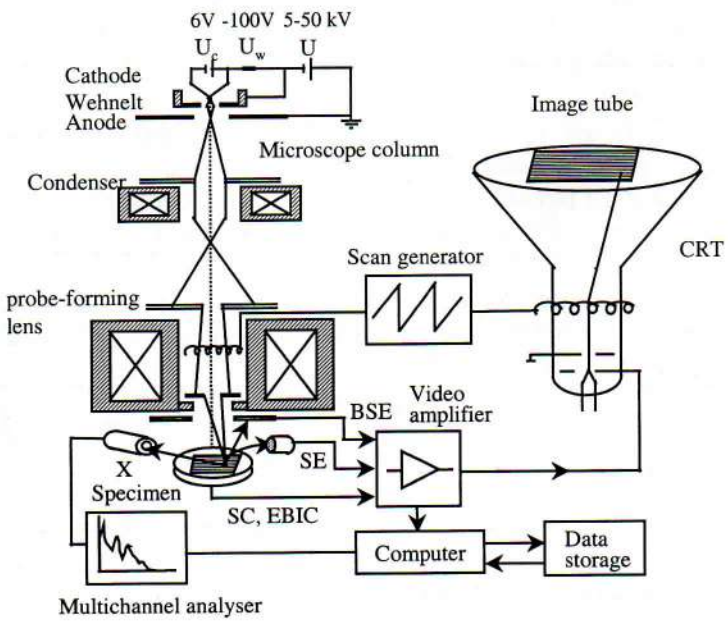

Figure 3.5. *Principles of the scanning electron microscope (BSE=backscattered electrons, SE=secondary electrons, SC=specimen current, EBIC=electron-beam-induced current, X=x-ray, CRT=cathode-ray tube)* [48].

Scanning electron microscopy studies were carried out using a Zeiss DMS 960 microscope. To avoid charging effects, the samples were coated with thin gold film.

3.2.5. Transmittance measurements

In order to demonstrate the presence of the dye in the films, it was necessary to measure the spectral transmittance for the films in the visible range. The spectrophotometer used is a double beam Perkin Elmer Lambda 9 instrument. The instrument has two radiation sources: a deuterium lamp and a halogen lamp. These two sources are prealigned, and the spectrophotometer has automatic source change during the registration of the spectrum. The detecting system was a side window photomultiplier system for the UV/VIS range and a PbS detector for the near-infrared range. For transmittance measurements, the spectrophotometer was operated with a normal incidence beam with an empty reference.

3.3. Electrochemical and photoelectrochemical characterization

Mostly one is interested in reactions or events that occur at a single surface of the electrode but, as we mentioned before, in electrochemistry we cannot deal with an isolated boundary because we always use a reference to control the potential of the system. Under some conditions we can use either two-electrode cells, where the studied electrode is called the working electrode (WE) and an ideal nonpolarizable electrode of known potential called the reference electrode (RE), or three-electrode cell arrangements where a third electrode called an auxiliary or counter electrode (CE) is used. A potentiostat is used to monitor the potential difference between the WE and the RE. With high input impedance, a negligible current is drawn through the RE. Fig. 3.6 depicts the electrodes and illustrates the principles of the two and three-electrode cells.

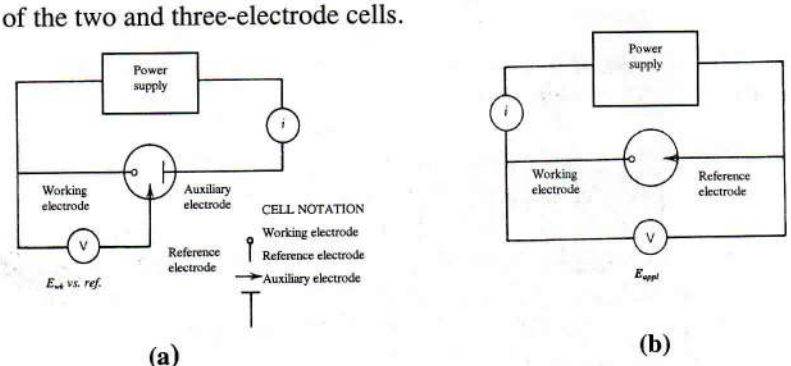

Figure 3.6. (a) *Two-electrode cell and (b) three-electrode arrangements.*

3.3.1. Cyclic voltammetry

Cyclic voltammetry [49,50] is commonly chosen as a technique to apply to a new system, because it gives information about potentials where reactions take place, crystallinity of the

sample, the intensity of the current involved in the reactions, as well as kinetic information of the process. So, a fingerprint of the system is obtained.

In cyclic voltammetry the current is recorded as a function of potential, the WE is controlled by a potentiostat and the potential is often varied linearly with time with a constant sweep rate as shown in Fig. 3.7a. A typical cyclic voltammogram is shown in Fig 3.7b. At the beginning the electrolyte only has oxidized species and there is no reaction for the initial potential E_1, so only non-faradic currents flow. When the electrode potential decreases the oxidized species at the surface are reduced. When the *WE* potential is negative enough to make the concentration of the oxidized species zero, the current reaches the maximum of the cathodic peak and the diffusion effects set in. When the reverse of the scan starts (E_2 at time τ) there is a large concentration of the oxidizable anion in the electrode's vicinity and the reduced species are oxidized in a similar manner and we will see an anodic peak.

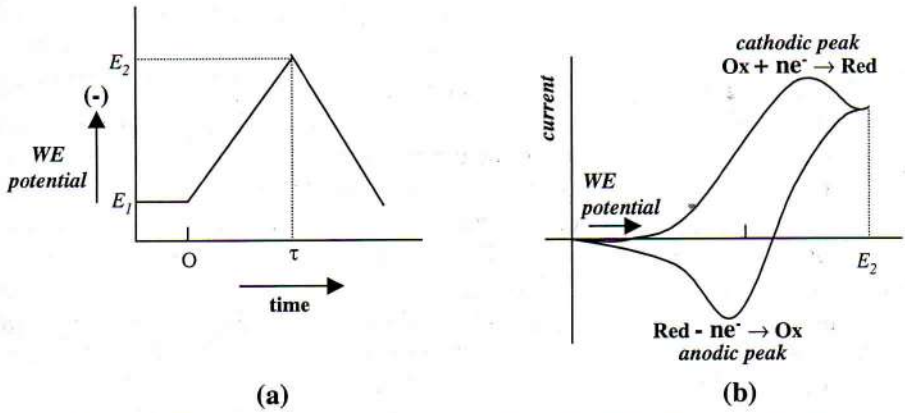

Figure 3.7. *(a) The change of potential with time and (b) the resulting current vs. potential curve in a cyclic voltammogram.*

Cyclic voltammetry was employed to obtained data on film porosity by studying the effect of adsorbed viologen molecules on the titanium oxide and by considering an electroreactive-nerstian reaction. The titanium oxide film was first sensitized with the viologen N(phophono-3-propyl),N'-methyl-4,4'-bipyridinium dibromide by soaking the film in a $1x10^{-5}$M solution in ethanol. Prior to sensitization the titanium oxide film was kept in air at 350°C for 5 minutes. Then it was dipped into the viologen solution while it was still warm (80°C) and the film was kept immersed one day.

A roughness factor was obtained from measurements in a three-electrode electrochemical cell connected to a multichannel ECO Chemie Autolab/GPES electrochemical interface. The working electrode consisted of glassy carbon, and the reference electrode was Ag/AgCl in saturated LiCl in anhydrous acetonitrile. The electrolyte was tetrabutylammonium tetrafluoroborate in acetonitrile. All electrochemical measurements were performed under dry conditions in a glove box containing Ar.

[illegible] photon-to-current efficiency

[illegible] photon-to-current efficiency (IPCE) [33] was determined from experiments using [illegible] and two-electrode cells. Spectral data were registered point by point, taking random [illegible] of the wavelength to avoid systematic errors during the measurement. IPCE was [illegible] by

$$IPCE = \frac{1240 i_{ph}}{P\lambda}, \qquad (3.4)$$

[illegible] (i_{ph} (in μA/cm^2) and P (in μW/cm^2) are photocurrent and power of the incident [illegible] per unit area, respectively, and λ (in nm) is the wavelength of the light. No [illegible] were made for absorption and reflection in the substrate. The light source was a [illegible] W Xe lamp whose beam passed through an 80-mm-thick water filter into a high-[illegible] monochromator (Schoeffel GM 252) and a focusing lens. The beam was then split [illegible] parts by a quartz window. One of the parts (a small fraction) was directed toward a [illegible] reading the intensity, and the other part toward the sample. The system was [illegible] using an optical power meter (Photodyne Model 44XL) with a silicon photodiode [illegible] 400 AS) radiometric sensor head

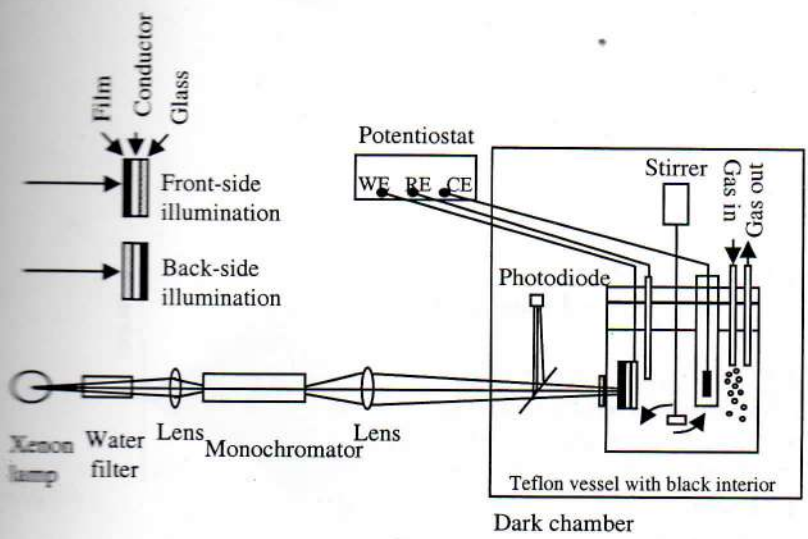

[illegible] 3.8. *Schematic of the experimental set-up for IPCE measurements for three-[illegible] measurements.*

Three-electrode measurements on *unsensitized* samples (without dye) were performed in [illegible] set-up shown in Fig 3.8 [51]. The titanium oxide film was placed as working electrode [illegible] three-electrode system. The counter electrode was a net of Pt enclosed in a glass tube [illegible] frit glass at its extreme end, and the reference was a saturated Calomel electrode. A

general-purpose potentiostat (Princeton Applied Research, Model 173) was used for the electrochemical measurements. The electrolyte was 0.1M KI in water purged with nitrogen. The pH was adjusted to 6.6 by 0.02M potassium phosphate buffer.

Action spectra were recorded in the ultraviolet wavelength range, at $280 < \lambda < 400$ nm. At the beginning of each recording session, the working electrode was biased to 0.3 V until it attained a steady state value of the dark current.

Two-electrode measurements were performed in a sandwich cell in which the *dye-sensitized* (with dye) titanium oxide film was the working electrode. The sensitization was made with a $5x10^{-4}$M solution of cis-dithiocyanato-N-bis(2,2'-bipyridyl-4,4'-dicarboxylic acid) ruthenium (II) in ethanol. The procedure was the same as for viologen incorporation (Sec 3.3.1). Excess dye was removed by subsequent rinsing with ethanol. The electrode was pressed together with a Pt foil using a spring. The electrolyte was 0.5M LiI/0.05M I_2 in acetonitrile. The IPCE for the electrodes was measured in the short circuit mode for back-side illumination. Action spectra were recorded in the visible wavelength range ($400 < \lambda <$ 800 nm)

4. EXPERIMENTAL RESULTS

Titanium oxide films were prepared by sputtering on a smooth ITO (In_2O_3:Sn) and a rough SnO_2:F which gives films with completely different characteristics (figure 4.1 shows the AFM images of the bare substrates). For this reason this chapter is divided into two parts which cover the films deposited on ITO and the films deposited on SnO_2:F. Each part contains preparation conditions, structural characterization and incident photon-to-current efficiency data (IPCE). In addition, the influence of the dye is studied on the films deposited on SnO_2:F

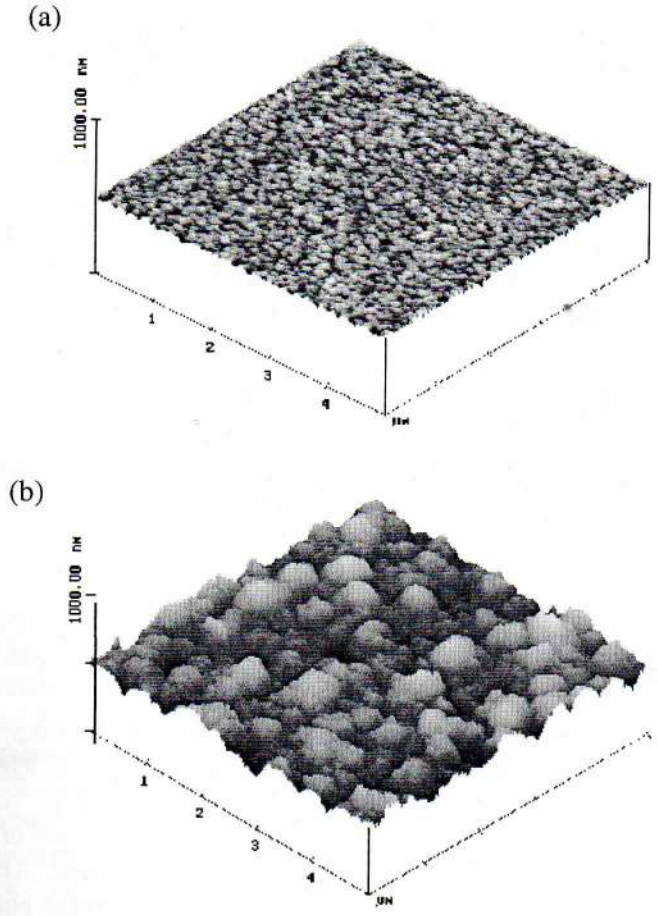

Figure 4.1 *Atomic force micrographs of ITO (a) and SnO_2:F (b).*

4.1. Data for sputter Ti oxide deposited on ITO

4.1.1. Sputter deposition

Ti oxide films were grown using reactive DC magnetron sputtering. Section 3.1.5 described this technique and the sputtering system used in this work. The transparent ITO-coated substrate had a resistance/square of 14 Ω.

After evacuation to ~10^{-7} Torr by turbo molecular pumping, sputtering took place in an atmosphere of Ar (99.998%) mixed with O_2 (99.998%). The O_2/Ar gas flow ratio was kept constant at a value Γ during the film deposition. The substrate temperature τ_s was controlled by a resistive heater, and the film uniformity was assured by rotating the substrate.

In order to determine the maximum IPCE values, a series of coatings were made under different conditions. Table 4.1 summarizes typical sputter conditions for titanium oxide deposition.

Table 4.1 *Sputter conditions for Ti oxide deposition*

Target material	Ti (99.9%)
Target size	ϕ 5 cm
Target - substrate distance	13 cm
DC power	400 - 650 W
Sputtering gas pressure	12 mTorr
O_2/Ar ratio (Γ)	0.050 - 0.078
Substrate temperature(τ_s)	room temperature (R.T.) - 250°C
Sputtering time	10 - 35 minutes
Pre-sputtering time	10 minutes

4.1.2. X-ray diffraction data

Titanium oxide films were investigated by XRD using an instrument described in section 3.2.2. The thickness for all of these films was ~220 nm and Γ was 0.05. Figure 4.2 displays XRD data for titanium oxide films deposited at different values of τ_s. No distinct peaks from titanium oxide were obtained at τ_s < 100°C. However, an increase of τ_s to 150°C led to the appearance of one peak assigned to an anatase (101) reflection. This peak became more prominent at τ_s = 200°C. No diffraction peaks due to the rutile phase were visible until τ_s = 250°C; over this temperature a (101) reflection shows up. Crystallite sizes, deduced from the anatase (101) peak, for films deposited at 150, 200, and 250°C were 7, 13, and 18 nm, respectively. The crystallite size corresponding to the rutile, deduced from

(101) peak, was ~15 nm. These data are in agreement with those obtained by Strømme et al.[52] for titanium oxide films.

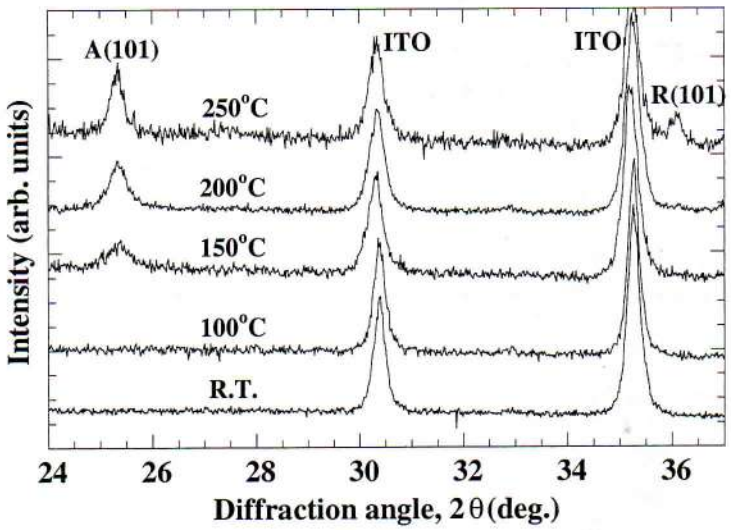

Figure 4.2 *X-ray diffractograms for DC-sputtered titanium oxide films on ITO precoated glass substrates at different temperatures: room temperature (R.T.), 100, 150, 200 and 250°C. Diffraction peaks are assigned to different reflections in the anatase (A) and rutile (R) structure.*

4.1.3. Incident photon-to-current efficiency

Incident photon-to-current conversion efficiency (IPCE) was measured in a three-electrode set-up as it was described in section 3.3.2. The following section illustrates how the IPCE is influenced by different deposition parameters, such as the substrate temperature, the O_2/Ar gas flow ratio and the sputtering time (i.e., the film thickness).

The influence of the substrate temperature is shown in Figs. 4.3a and 4.3b which display IPCE data for front-side illumination (light directly onto the film) and back-side illumination (through the conducting glass) respectively, for samples deposited at different values of τ_s (the same temperatures as those shown for the films at Fig. 4.2). The film deposited at τ_s = 250°C obtains a maximum photoresponse (~14%) at λ = 300 nm. The general trend, common to all samples, is that the quantum efficiency has a maximum value at λ = 300 nm, and that the photoresponse is higher as the deposition temperature is larger. The IPCE profiles for back-side illumination (Fig. 4.3b) display a similar correlation between τ_s and IPCE, but absorption effects due to the glass substrate can be seen for $\lambda <$ 350 nm.

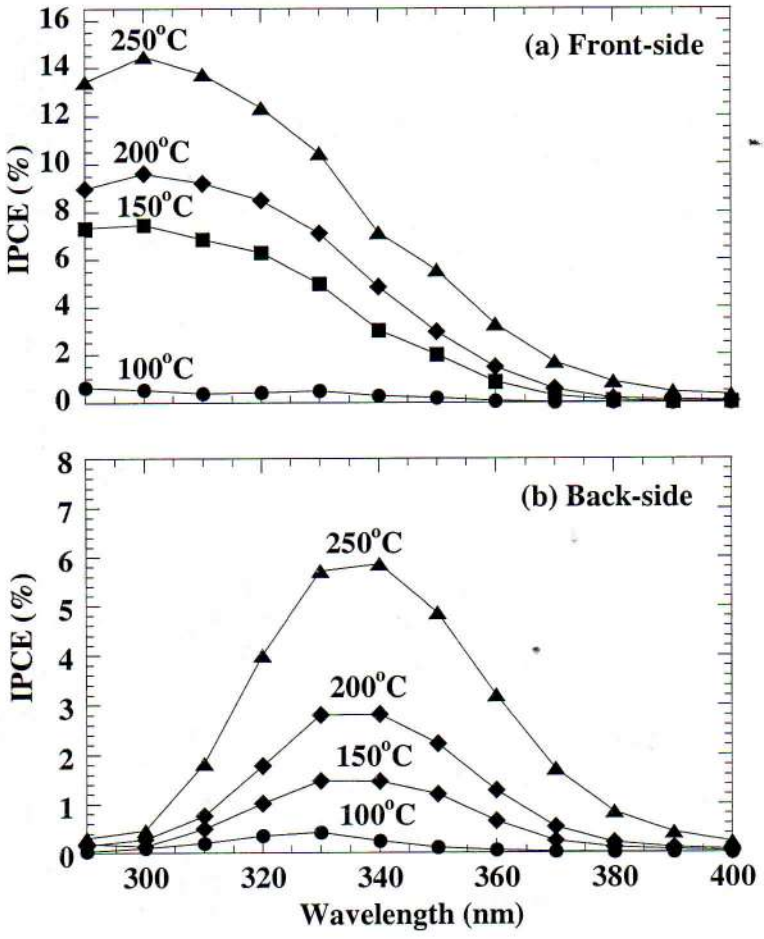

Figure 4.3 *Spectral incident photon-to-current efficiency (IPCE) for front-side (part a) and back-side (part b) illumination of titanium oxide films sputter deposited onto ITO coated glass substrates at the shown temperatures.*

Even though the magnitude of the photoresponse is rather low, the striking observation is that a mixture of anatase and rutile phases generates the best IPCE in our sputter deposited titanium oxide films.

Considering now the role of the O_2/Ar ratio, Figs. 4.4a and 4.4b show IPCE spectra for front-side and back-side illumination of samples deposited at τ_s = 250°C at a total pressure of 12 mTorr. This pressure was found to give the optimized photoresponse, at least in the range between 10 and 13 mTorr. The films were about 600 nm thick and the deposition rate was 0.5 nm/s; the only exception being that the film deposited at Γ = 0.07 was ~450 nm thick with a deposition rate of 0.4 nm/s.

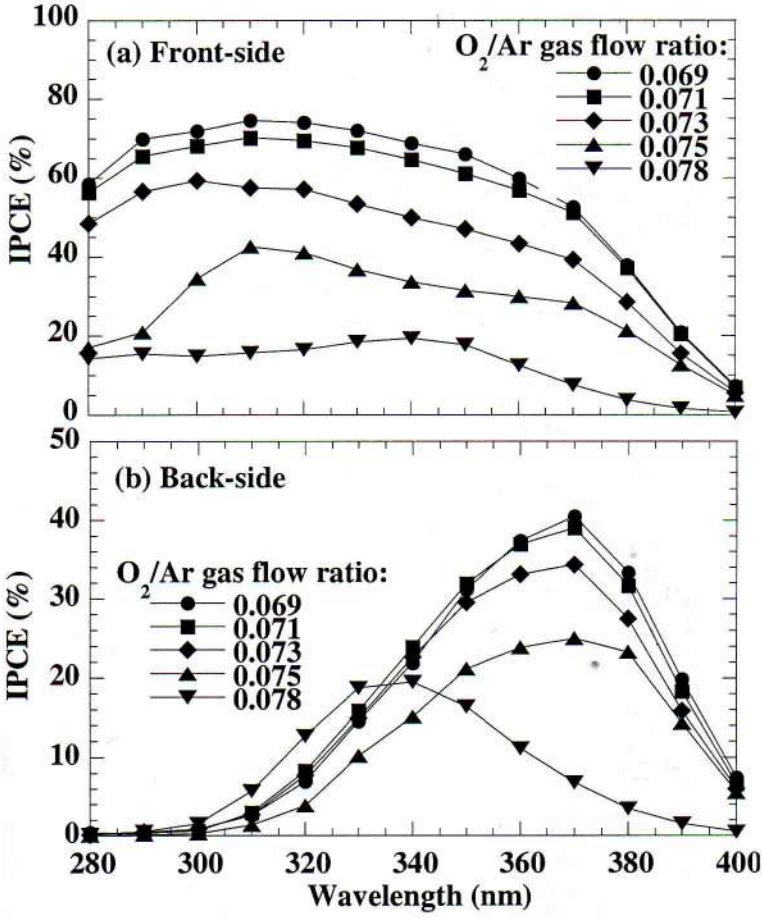

Figure 4.4 *Spectral incident photon-to-current efficiency (IPCE) for front-side (part a) and back-side (part b) illumination of titanium oxide films sputter deposited onto ITO coated glass substrates at the shown O_2/Ar gas flow ratios.*

The quantum efficiency for front-side illumination of the sample deposited at $\Gamma = 0.069$ reaches a maximum of as much as 75% at $\lambda = 310$ nm (Fig. 4.4a). This value is higher than those reported for polycrystalline films [53,54]. Data for front-side illumination onto films deposited at $\Gamma = 0.071$ and $\Gamma = 0.073$, show that they have the same spectral features as those films deposited at $\Gamma = 0.069$, but the enhanced oxygen admixture produces a systematic decrease in the photoresponse. Films deposited at even higher O_2 content display the same trend in the spectral photoresponse, but it is noteworthy that the film deposited at $\Gamma = 0.075$ yields two peaks in the IPCE at the wavelengths 370 and 310 nm (see figure 4.4a), while the film deposited at $\Gamma = 0.078$ shows only one maximum at $\lambda = 340$ nm. In the case

of back-side illumination, the distinctive spectral features upon increased Γ are decreased photoresponse and a shift of the maximum IPCE toward shorter wavelengths.

The influence of film thickness is described in Figs. 4.5a and 4.5b, showing IPCE spectra for front-side and back-side illumination of samples deposited at τ_s = 250°C for different periods of time in order to obtain a range of thicknesses. The deposition rate and Γ were 0.5 nm/s and 0.074, respectively. Figure 4.5a gives clear evidence of the importance of having a suitable film thickness. The thinnest film, with a thickness of 279 nm, displays a maximum photoresponse of 43% at λ = 300 nm, while the 432-nm-thick film has a maximum photoresponse of 67% at the same wavelength. Back-side illumination produces similar trends for the relation between IPCE and film thickness but also shows a shift of the maximum IPCE values towards longer wavelength as the film becomes thicker.

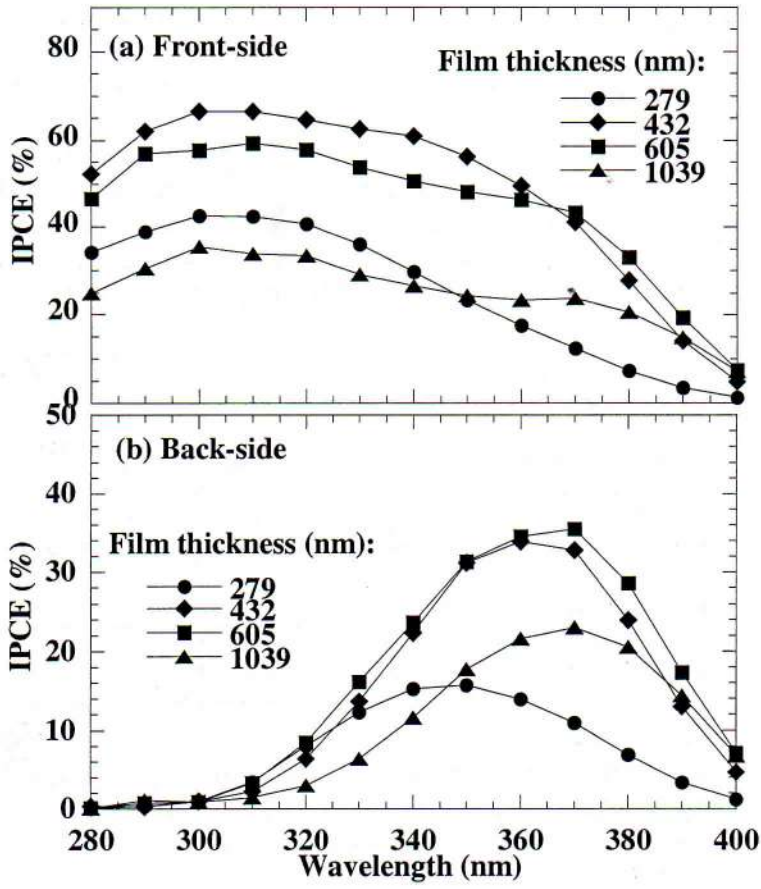

Figure 4.5 *Spectral incident photon-to-current efficiency (IPCE) for front-side (part a) and back-side (part b) illumination of titanium oxide films, having different thicknesses, sputter deposited onto ITO coated glass substrates.*

4.2. Data for sputter Ti oxide deposited on SnO_2:F

4.2.1 Sputter deposition

The only difference between sputter conditions of the films deposited on SnO_2:F and the ones described in section 4.1. is the sputtering time. In this section data from films deposited as long as 5 hours will be presented.

4.2.2. Structure and morphology of the films

4.2.2.1 X-ray diffraction data

Figure 4.6 shows grazing incidence X-ray diffractograms for titanium oxide films sputtered onto conducting glass kept at different values of the substrate temperature τ_s. The thickness for all of the films is ~260 nm. No diffraction peaks due to titanium oxide were visible for samples deposited at room temperature, and similar results were obtained for τ_s = 100°C. By setting the substrate temperature at 200°C, however, one peak corresponding to anatase (101) reflections became apparent at 2θ = 25.3°. For τ_s = 250°C, there is clear XRD evidence in favor of an anatase-rutile mixture. Applying Scherrer's formula to the anatase (101) peak for films deposited at τ_s = 200°C, the grain size was found to be about 10 nm. For the film deposited at τ_s = 250°C, the grain size derived from the same anatase peak was ~30 nm, whereas the rutile (110) and (101) peaks corresponded to ~8 nm.

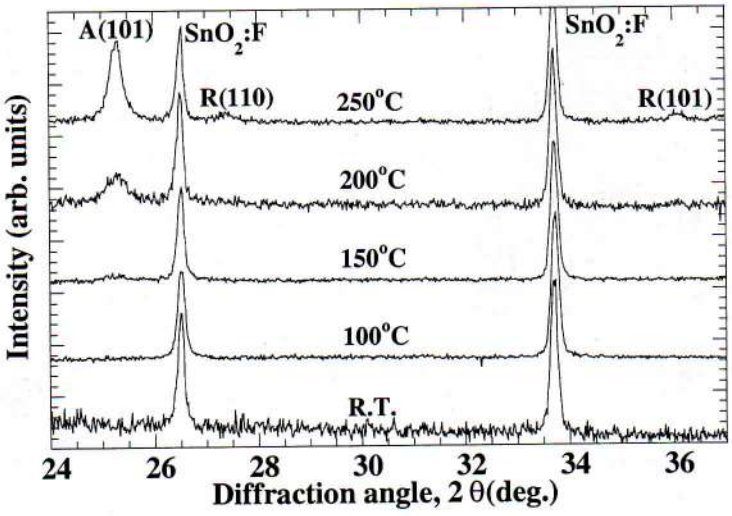

Figure 4.6 *X-ray diffractogram for titanium oxide films on SnO_2:F coated glass substrates. The substrate was kept at room temperature (R.T) and at three elevated temperatures during the sputter deposition. The diffraction peaks are assigned to different reflections in the anatase (A) and rutile (R) structure.*

Figure 4.7 shows data for films with thicknesses of 8, 6.7 and 1.9 μm. The diffractograms display two prominent peaks due to the rutile (110) and (101) reflections, as well as a small peak assigned to anatase (101) [43]. The film with $d \approx 4.2$ μm displayed an unexpectedly strong anatase peak. The different crystalline structures may be associated with the fact that the film with $d = 4.2$ μm was deposited at 0.3 nm/s, whereas the other film was made with a deposition rate of 0.42 nm/s. Diffraction features due to SnO_2:F were visible in all cases.

Scherrer's equation [44] was applied to the rutile (101) peaks for all of the samples in order to assess the mean grain size. The grain size was found to vary monotonically with film thickness and, somewhat unexpectedly, the thickest films had the smallest grain size. Specifically, the films whose thicknesses were 1.9 and 8 μm had mean grain sizes of 25 and 18 nm, respectively. These magnitudes of D are in the same range as the microcrystallite dimensions of titanium oxide electrodes earlier prepared from nanoparticles [55].

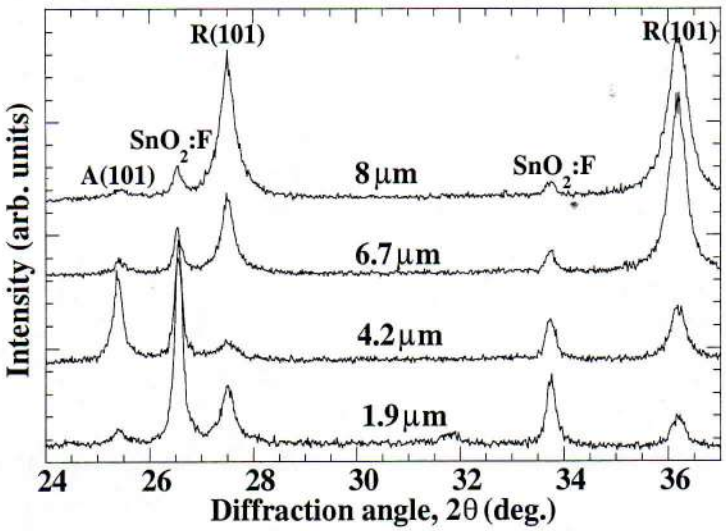

Figure 4.7 *X-ray diffractograms for titanium oxide films on glass substrate precoated with SnO_2:F. Data are given for different film thicknesses. The diffraction peaks are assigned to the shown reflections in the anatase (A) and rutile (R) structure in titanium oxide. Additional peaks originate from SnO_2:F.*

4.2.2.2. AFM and SEM data

AFM was used to investigate the morphology of titanium oxide films deposited onto SnO_2:F. AFM measurements were made using a Nanoscope III with an etched silicon cantilever.

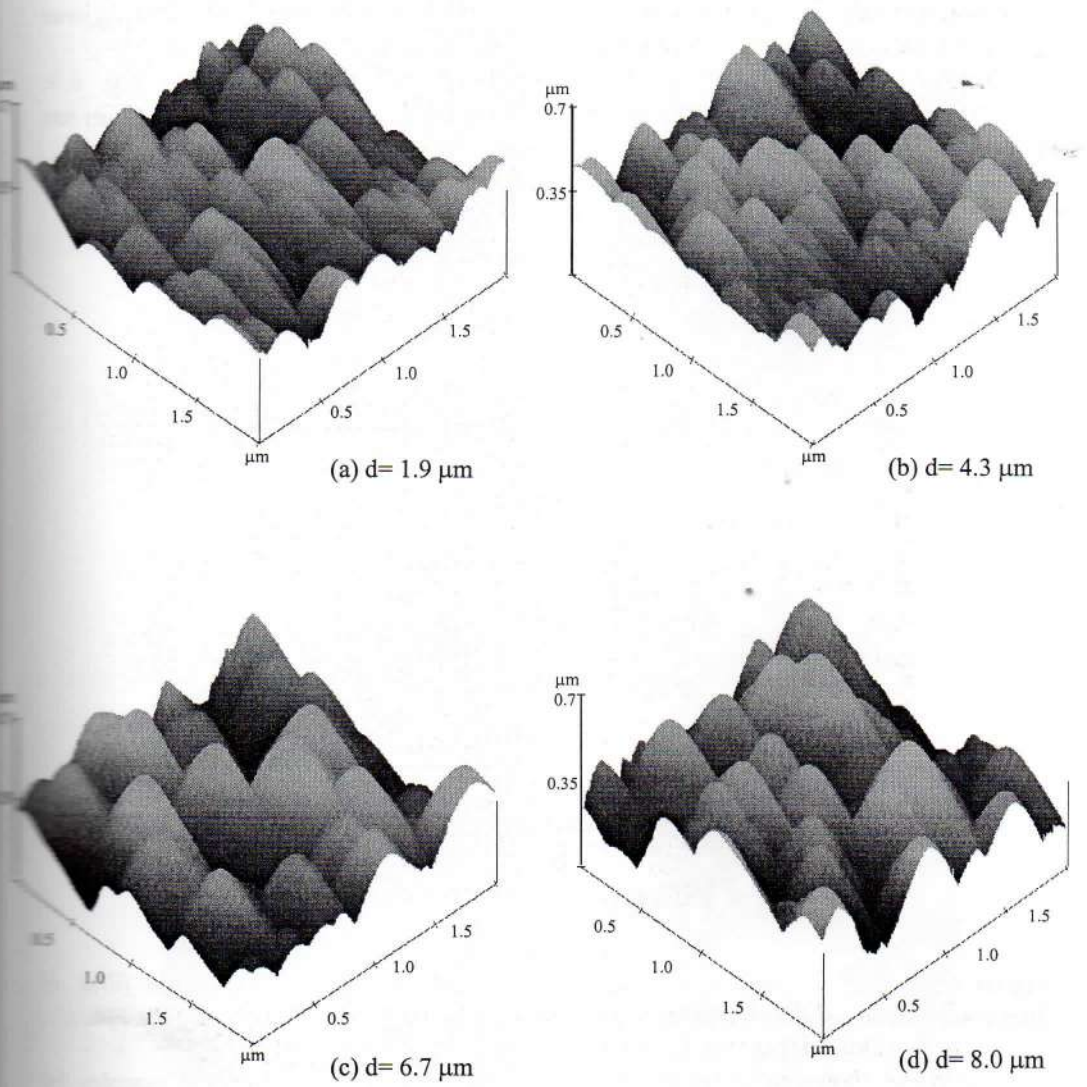

Figure 4.8 *Atomic force micrographs taken on Ti oxide films having the shown values of the thickness.*

Data were taken in ambient air with a contact force of about 10^{-7} N. Scans were extended over areas of 2x2 μm. Figure 4.8 shows AFM images. The surface structure is represented by domains that are about 0.25 μm in diameter for the 1.9 μm thickness film and which increase to 0.4 μm for the 8 μm film. The rms roughness, denoted R_{AFM}, was obtained by employing software supplied with the instrument [56].

The roughness grows larger in the thicker films, as seen from Fig. 4.9. Specifically, the film with d = 1.9 μm has R_{AFM} = 49 nm and the film with d = 8 μm has R_{AFM} = 91 nm. The increment of the R_{AFM} is associated principally to the domain size.

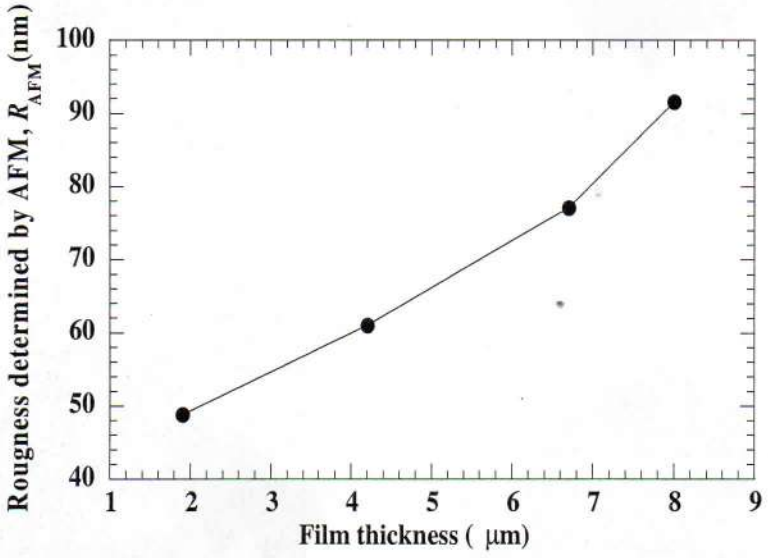

Figure 4.9 *Rms roughness as determined from AFM for titanium oxide films of different thicknesses. Dots represent data and lines were drawn as a guide to the eye.*

Scanning electron micrographs were taken from the surface of the samples by using a Zeiss DSM 960 instrument operating at 20 kV. Figures 4.10a-d show SEM images of the surfaces for four samples with different film thicknesses, deposited onto the SnO_2:F coated glass. Rough surfaces with well-rounded protruding nodules are apparent. The nodular size goes up with increasing film thickness from ~ 0.2 μm at $d \approx 1.9$ μm to ~ 0.5 μm at $d \approx 8$ μm.

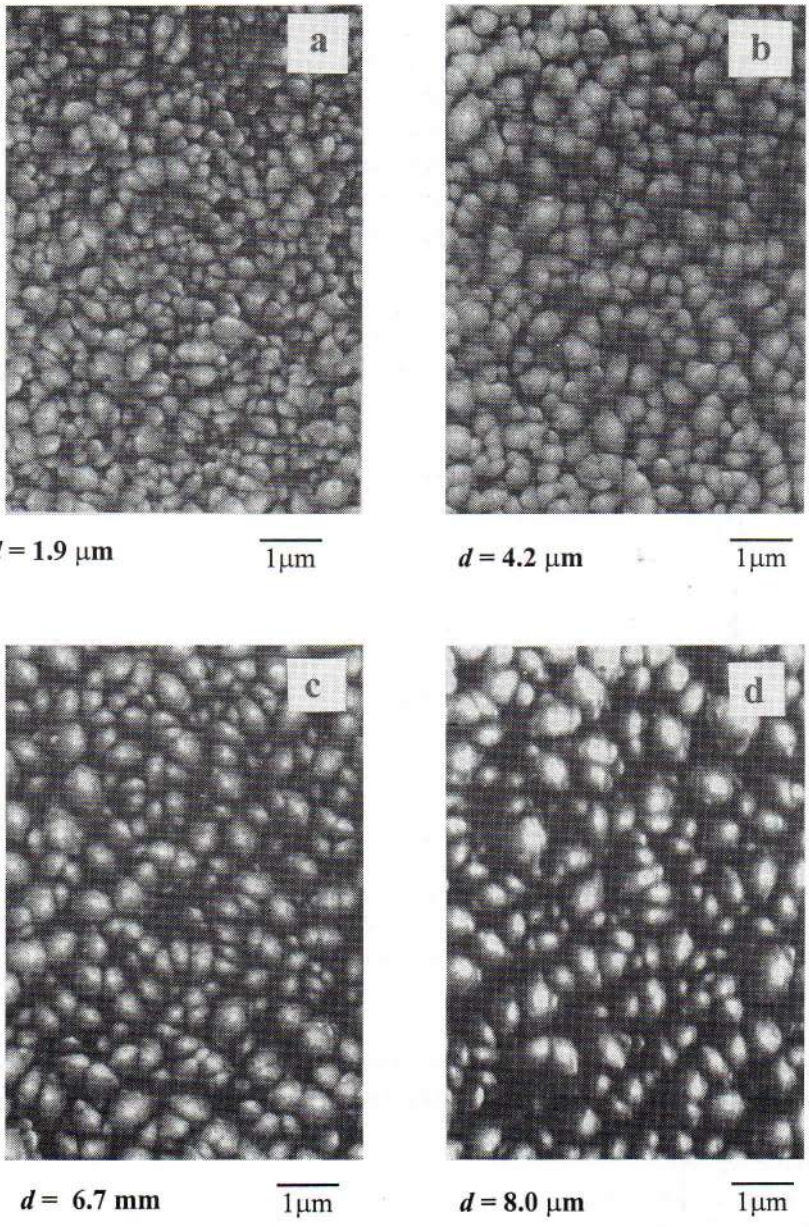

Figure 4.10 *Scanning electron micrographs of Ti oxide films having values of the thickness d.*

4.2.3. Spectral transmittance data

The unambiguous presence of the dye on the films was probed by spectral optical transmittance measurements in the visible wavelength range, i.e., at $400 < \lambda < 800$ nm. Figure 4.11 shows the transmittance for the 170-nm-thick and the 1040-nm-thick titanium oxide films with and without dye. The films are strongly light scattering. The maximum transmittance of the 170-nm-thick film (with and without dye) is around 0.64 at $\lambda = 750$ nm, while the 1040-nm-thick film has a maximum transmittance (in the absence of dye) of no more than 0.44 at the same wavelength. The dye absorption band for the 1040-nm-thick sensitized electrode is centered at 540 nm in wavelength, and may be broader than the absorption band apparent in the 170-nm-thick electrode. The data in Fig. 4.11 give clear evidence in favor of a film thickness dependence of the dye incorporation.

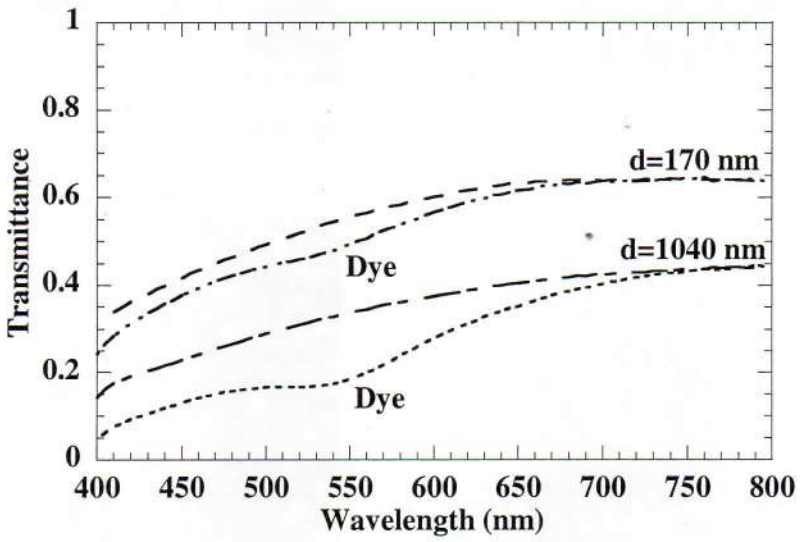

Figure 4.11 *Total spectral transmittance through SnO_2:F coated glass substrates with sputter deposited titanium oxide films having the shown thickness d. Data were recorded with and without dye sensitization.*

4.2.4. Cyclic voltammogram data

Figure 4.12 shows cyclic voltamograms taken at a voltage sweep rate of 10 mV/s for samples with different film thicknesses. The lower peak at -0.82 V represents the first reduction peak of the viologen, and the upper peak at -0.72 V is the oxidation wave of the reduced viologen.

Integration of the CV curves such as those in figure 4.12 gave a maximum charge Q for reducing (or oxidizing) the viologen. The surface concentration Γ was then calculated from

$$\Gamma = \frac{Q}{FnA}, \tag{4.1}$$

where F is Faraday's constant, n is the number of the electrons exchanged during the redox reaction, and A is the area of the electrode. The conditions for this work correspond to $n = 1$. The roughness factor can be obtained from

$$\rho_{cv} = \frac{\Gamma}{C}, \tag{4.2}$$

where C is the fraction of the surface covered by the viologen molecules. An empirical value of C is obtained from the fact that a coverage of $\sim 10^{-10}$ mol/cm^2 corresponds approximately to one monolayer [57]. Evaluations of ρ_{cv} by this procedure yielded the quantities illustrated in Fig. 4.13.

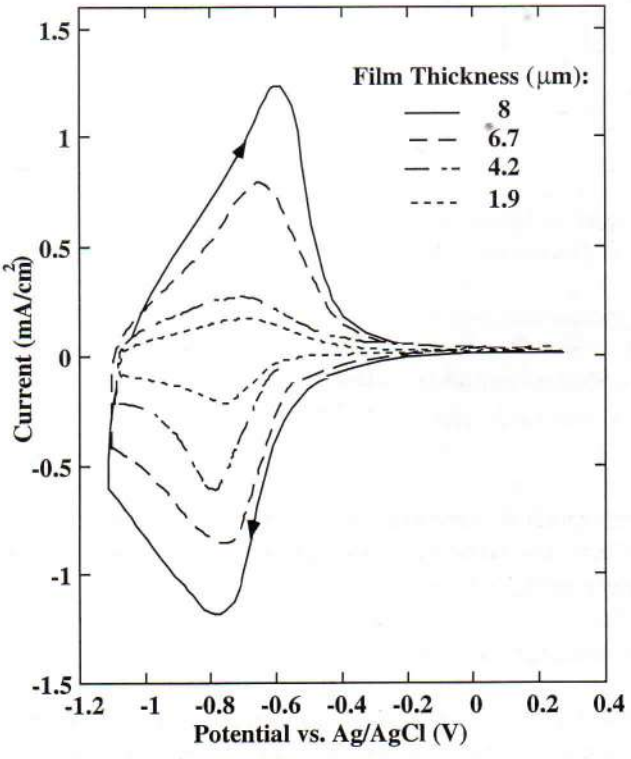

Figure 4.12 *Cyclic voltammograms for viologen-containing titanium oxide films with different thicknesses. The voltage sweep rate was 10 mV/s. Arrows denote sweep direction.*

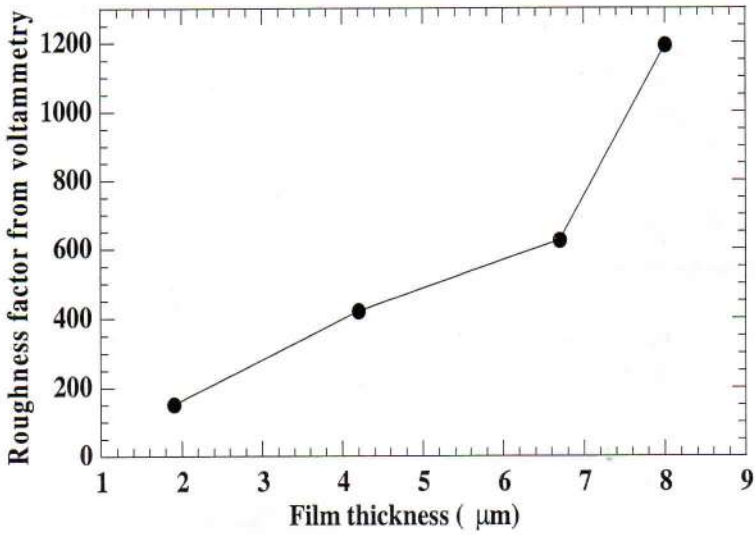

Figure 4.13 *Roughness factor based on cyclic voltammetry for titanium oxide films with different thickness. Dots represent data and lines were drawn as a guide to the eye.*

4.2.5. Incident photon-to-current efficiency

The influence of substrate temperature is shown in figures 4.14a and 4.14b which display the IPCE data for front-side illumination (light directly onto the film) and back-side illumination (light through the conducting glass) in the three-electrode set-up for a series of *unsensitized* titanium oxide films deposited at different substrate temperatures. The thickness for all the films is ~260 nm. All spectra were measured only in the ultraviolet range, i.e., at $280 < \lambda < 400$ nm. The action spectra for front-side and back-side illumination of the corresponding titanium oxide electrodes show a number of common features. Specifically, the photoresponse is higher the higher the substrate temperature used for the deposition of the film, and the spectrum for front-side illumination of the film deposited at $\tau_s = 250°C$ yields 11% as the maximum photoresponse at $\lambda = 300$ nm, while the maximum value obtained for the film obtained at $\tau_s = 100°C$ is only around 1%. The action spectra for the back-side illumination display distinctive features due to the absorption at $\lambda < 350$ nm in the transparent conducting layer. Similar data have been recorded for polycrystalline films deposited on ITO.

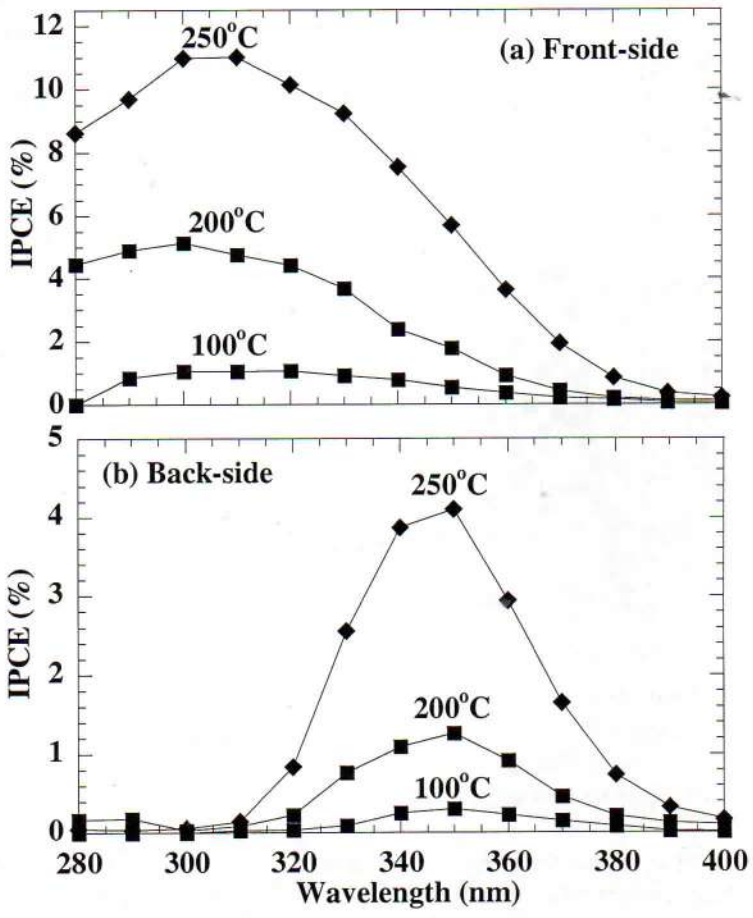

Figure 4.14 *Spectral incident photon-to-current efficiency (IPCE) for front-side (part a) and back-side (part b) illumination of titanium oxide films sputter deposited onto SnO_2:F coated glass substrates at the shown temperatures. The measurements were performed in a three-electrode cell with an electrolyte consisting of an aqueous of 0.1M KI solution purged with nitrogen.*

Two-electrode measurements were performed with *dye-sensitized* titanium oxide films as described in section 3.3.2. The electrolyte was 0.5M LiI/0.05M I_2 in acetonitrile. A two-electrode solar cell set-up was used to measure IPCE spectra in the ultraviolet and visible wavelength ranges for different thickness of titanium oxide electrodes. Data are reported in Fig. 4.15 where part (a) refers to one series of titanium oxide samples sputter

deposited in direct succession so that films with different thicknesses were obtained. The film with d = 1040 nm has a maximum IPCE of about 20%, while the thinner films display IPCEs that decrease with diminishing thickness. Figure 4.15b contains results for another series of titanium oxide films analogous to the one reported on in Fig. 4.15a. By comparing the two sets of data, it is possible to verify the reproducibility of the photoresponse with the change of film thickness. Furthermore, it is found that the 1300-nm-thick titanium oxide film in Fig. 4.15b has a maximum IPCE of about 30%, which is comparable to data for films prepared from nanoparticles [53].

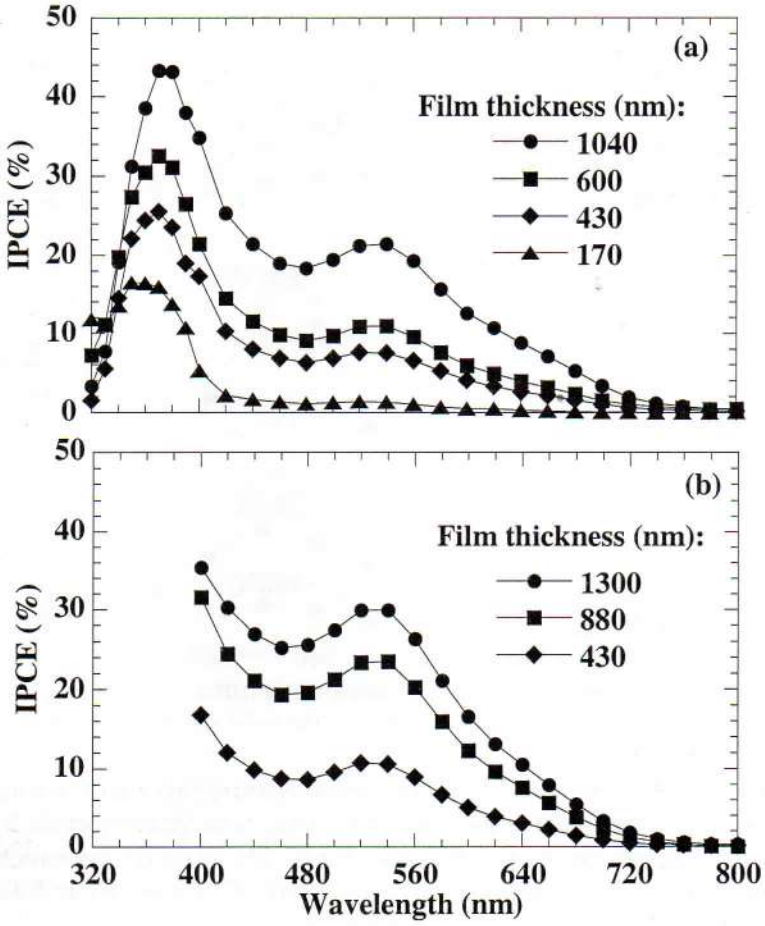

Figure 4.15 *Spectral incident photon-to-current efficiency (IPCE) for back-side illumination of titanium oxide films sputter deposited onto SnO_2:F coated glass substrates. The data in parts (a) and (b) refer to two separate series of samples, each comprising a range of film thicknesses. The measurements were performed in a two-electrode system employing acetonitrile with a LiI/I_2 solution as the electrolyte.*

Figure 4.16 shows spectral action spectra for a series of films having different thicknesses. The data for all of the samples displays similar features and, in general, the IPCE rises with increasing film thickness. The data consistently displays a peak centered at ~ 530 nm; the feature becomes less distinct in the thicker films.

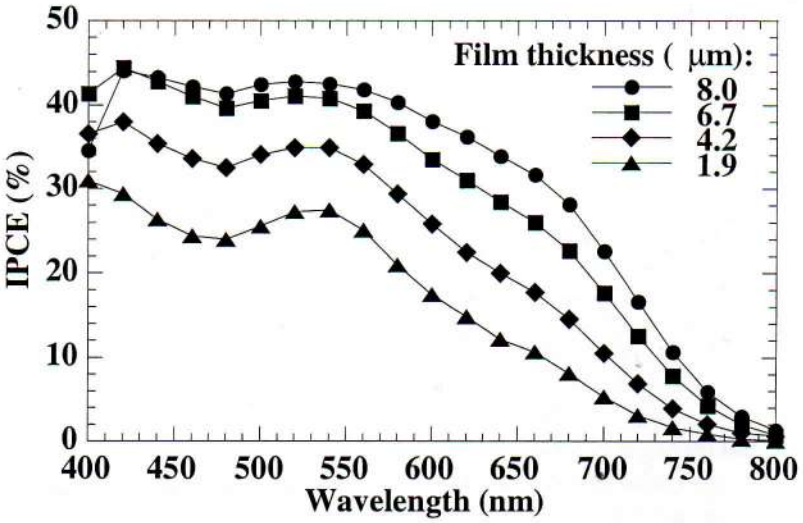

Figure 4.16 *Spectral incident photon-to-current efficiency (IPCE) for the titanium oxide films with the shown thicknesses. Dots represent data and lines were drawn as a guide to the eye.*

Figure 4.17 illustrates IPCE data for λ = 530 nm. The photoelectric efficiency goes up rather linearly with growing thickness, although some saturation may be apparent in the thickest films.

Figure 4.18 gives unambiguous evidence of the importance of having suitable film preparation conditions by showing results from a series of titanium oxide films deposited at different values of the O_2/Ar gas flow ratio. The rest of the parameters for the sputtering deposition were kept constant. All of these films were about 500 nm thick and were deposited at τ_s = 250°C. The film deposited at Γ = 0.06 shows a peak in the IPCE at λ = 540 nm equal to 7%. Decreasing Γ to 0.055 makes the peak in the IPCE rise to 9%, while lowing Γ still further makes the IPCE go down strongly. Clearly the composition of the sputtering plasma strongly affects the properties of the films and has a significant influence on the incident photon-to-current efficiency.

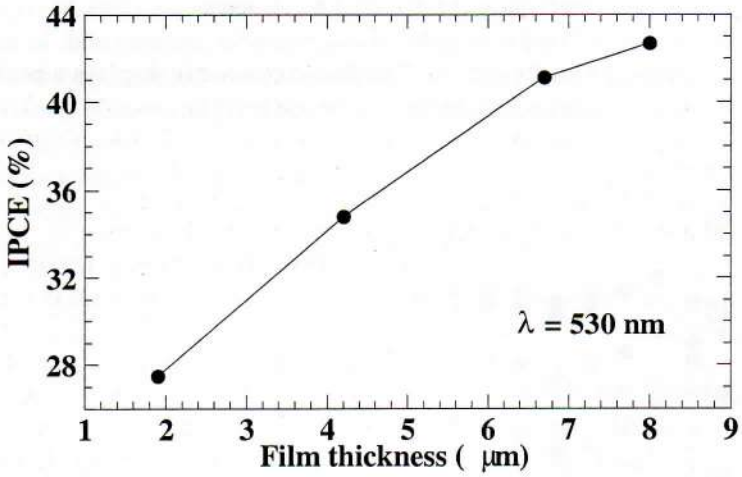

Figure 4.17 *Incident photon-to-current efficiency (IPCE) at a wavelength of 530 nm for titanium oxide films with different thicknesses. Dots represent data and lines were drawn as a guide to the eye.*

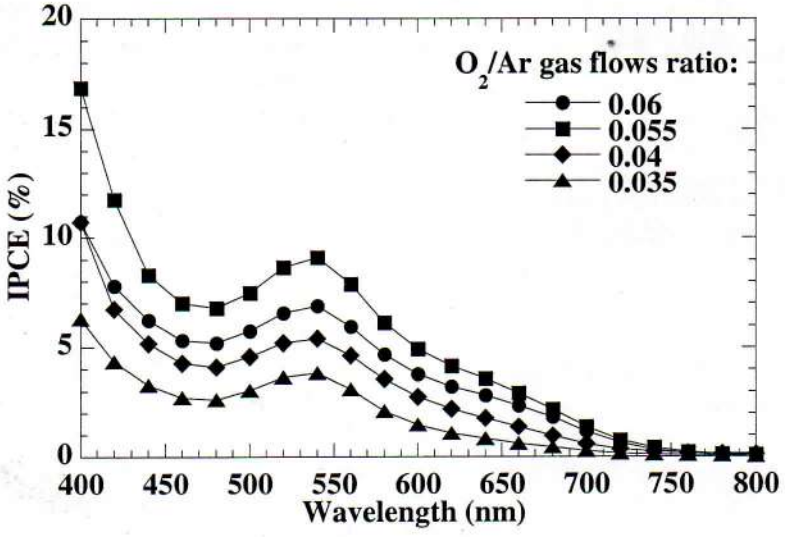

Figure 4.18 *Spectral incident photon-to-current efficiency (IPCE) for back-side illumination of titanium oxide films sputter deposited onto SnO_2:F coated glass substrates at the shown O_2/Ar gas flow ratios. The measurements were performed in a two-electrode system with acetonitrile employing a LiI/I_2 solution as the electrolyte.*

5. CONCLUDING REMARKS

Titanium oxide films were prepared by reactive DC magnetron sputtering on two types of conducting substrates: one being a smooth glass substrate precoated with a layer of transparent ITO (In_2O_3:Sn) having a resistance/square of 14 Ω, and the other a glass substrate precoated with a rough layer of SnO_2:F having a resistance/square of 8 Ω. These two types of substrate generate respectively two types of films which we can call smooth (deposited on ITO) and rough (deposited on SnO_2:F) films.

The coating deposited from the Ti target in oxygen/argon atmosphere is titanium oxide, which can have different phases depending on the temperature of the substrate during the deposition of the film.

For compact films a maximum photon-to-current efficiency (measured for front-side illumination) of 75% is obtained at a wavelength of 310 nm with a suitable stoichiometry (obtained by controlling the gas composition in the sputter plasma) and having a thickness of about 0.6 μm. The substrate temperature during film deposition was 250°C, which led to a mixed anatase-rutile structure.

Rough films can be sensitized with a dye. Thick dye-sensitized semiconductor films showed a photoresponse as high as 45% at a wavelength of 530 nm. Photoelectric conversion efficiency increased monotonically with increasing film thickness, although some saturation may be apparent for a thickness exceeding ~7 μm. Generally, the surface roughness as well as the internal porosity were enhanced in the thicker films.

The solar cells prepared by sputtering cannot yet compete in efficiency with those made by conventional colloidal methods, but the possibility of controlling the sputtering process to achieve different microstructures, and its proven industrial viability, makes the use of this technique for titanium oxide based solar cells of considerable interest for further studies.

6. SUMMARY OF THE APPENDED PAPERS

Paper I

Photoelectrochemical properties of polycrystalline Ti oxide thin films prepared by sputtering

Non-stoichiometric polycrystalline titanium oxide thin films were prepared by reactive DC magnetron sputtering of Ti in O_2+Ar onto Indium Tin Oxide (ITO) coated glass. Rutile and anatase phase films were obtained by heating the substrate during the deposition. Incident photon-to-current efficiency (IPCE) was studied as a function of several sputtering parameters such as temperature of the substrate, film thickness, and O_2/Ar gas flow ratio. The IPCE increased as the crystallinity of Ti oxide was systematically varied from amorphous to a mixture of anatase and rutile, and it was also enhanced in films deposited at low O_2/Ar ratios. The photoresponse was measured using a three-electrode set-up with an electrolyte consisting of an aqueous 0.1 M KI solution purged with nitrogen. Action spectra were scanned between 280 and 400 nm in wavelength. The photogenerated current was found to be highly dependent on the composition, thickness, and structure of Ti oxide films

Paper II

Photoelectrochemical studies of dye-sensitized polycrystalline titanium oxide thin film prepared by sputtering

Titanium oxide thin films were prepared by reactive DC magnetron sputtering of Ti in O_2+Ar onto SnO_2:F coated glass. A dye consisting of Cis-dithiocyanato-N-bis(2,2'-bipyridyl-4,4'-dicarboxylic acid) ruthenium (II) was incorporated by dipping the films into a solution of the dye in ethanol. The amount of dye incorporation was found to be highly dependent on the microstructure and the thickness of the film, as apparent from optical measurements. Incident photon-to-current efficiency was studied as a function of sputtering parameters using a three-electrode cell with an electrolyte consisting of an aqueous 0.1 M KI solution purged with nitrogen, as well as using a two-electrode system with acetonitrile with a LiI/I_2 solution as the electrolyte.

Paper III

Photoelectrochemical effect in dye-sensitized, sputter deposited Ti oxide films: The role thickness-dependent roughness and porosity

Ti oxide films were made by reactive DC magnetron sputtering onto electrically conducting glass substrates. The films were dye-sensitized with a Ru complex, thereby yielding nanocrystalline solar cells. We investigated the microstructure of the films by X-ray diffraction, scanning electron microscopy, atomic force microscopy, and cyclic voltammetry on viologen-containing samples. The internal surface area was enhanced with increasing film thickness, and that property could be correlated with an enlarged photoelectric conversion efficiency.

ACKNOWLEDGMENTS

First of all I would like to thank everyone who contributed to and supported this work in some way.
Especially I would like to thank my supervisors Claes Granqvist and Sten-Eric Linquist in Sweden, and Walter Estrada in Peru, for their guidance and help during the work and the writing.
I am grateful for the valuable discussions and suggestions from Gunnar Niklasson and Anders Hagfeldt every time when I needed.
I wish to thank Manfred Horn for the valuable comments on this summary.
I would like to thank the members in the Division of Solid State Physics and the Physical Chemistry, for a nice and friendly working atmosphere.
I wish to thank Juan for the very nice time we had working together.
I am also grateful to Lennart Hasselgren and all the staff at ISP for their constant help and the enthusiastic spirit.
I am grateful to my home University, the National University of Engineering, Peru, and especially the people from the Department of Thin Film at the Faculty of Science.
My endless gratitude to my parents, Marta and Armando, for their support and constant encouragement.
Finally, I thank God for being with me all the time and letting my life with my best friend, José, be happy.
This work is carried out at the Division of Solid State Physics, Department of Material of Science, The Ångström Laboratory, Uppsala University. It is financially supported by International Science Programs in Physics of Uppsala University.

REFERENCES

1. Matsubara H., Tanabe T., Moto A., Mine Y. and Takagishi S., *Solar Energy Materials and Solar Cells*, **1998**, 50, 177.

2. Takamoto T., Ikeda E., Kurita H. and Ohmori M., *Appl. Phys. Lett.* **1997**, 70, 381.

3. Espinoza R. and Horn, M. *Electrificación Rural con Sistemas Fotovoltaicos*, Universidad Nacional de Ingenería, Lima, Perú, **1992**.

4. Fujishima A. and Honda K., *Nature*, **1972**, 238,37.

5. Butler A., *J. Appl. Phys.*, **1977**, 48, 1914.

6. Gerischer H., *Electroanalytical Chemitry and Interfacial Electrochemistry*, **1975**, 58, 263.

7. Matsumura M., Matsudaira S., Tsubomura H., Masasuke T. and Yanagida H., *Ind. Eng. Chem. Prod. Res. Dev.*, **1980**, 19, 415.

8. O'Regan B. and Grätzel M., *Nature*, **1991**, 353, 737.

9. Hagfeldt A., Didriksson B., Palmqvist T., Lindström H., Södergren S. and Rensmo H. and Lindquist S.-E., *Solar Energy Materials and Solar Cells*, **1994**, 31, 481.

10. Barbé C., Arendse F., Comte P., Jirousek M., Lenzmann F., Shklover V. and Grätzel M., *J. Am. Ceram. Soc.*, **1997**, 80, 3157.

11. Roušar I., Rudolf M., Lukášek P., Kavan L., Papageorgiou N. and Grätzel M., *Solar Energy Mater. Solar Cells* **1996**, 43, 249.

12. Grünwald R. and Tributsch H., *J. Phys. Chem.* B **1997**, 101, 2564.

13. Dloczik, L., Ileperuma, O., Lauermann, I., Peter, L. M., Ponomarev, E. A., Redmond, G., Shaw, N. J., and Uhlendorf, I., *J Phys. Chem. B* **1997**, 101, 10281.

14. Zkeeruddin, S. M., Nazeeruddin, M. K., Pechy, P., Rotzinger, F. P., Humpmphry-Baker, R., Kalyanasundaram, K. and Grätzel, M., *Inorg. Chem.* **1997**, 36, 5937.

15. Wasa, K. and Hayakawa, S., *Handbook of Sputter Deposition Technology*, Noyes, Park Ridge, **1992.**

16. Westwood W. D., *Handbook of Thin Film Process Technology*, edited by Glocker D.A. and Shan S.I., IOP Publ. Bristol, **1998**.

17. Memming R., *Electrochimica Acta*, **1980**, 25, 77.

18. Matthews R., *Photochemical Conversion and Storage of Solar Energy*, eds. Pellizzetti E. and Schivello M., Kluwer, Dordrecht, **1991**.

19. Vinodgopal K., and Kamat P., *Chemtech.* **1996**, 26, 18.

20. Mills A. and Le Hunte S. *J. Photochem. Photobiol. A:Chem.*, **1997**, 108, 1.

21. Sze M., *Physics of Semiconductor Devices*, John Willey & Sons, New York, **1981**.

22. Morrison S., *Electrochemistry of Semiconductor and Oxidized Metal Electrodes.*, Plenum Press, New York, **1984**.

23. Kittel C. *Introduction to Solid Stated Physics.*, Jonh Willey & Sons, New York, **1976**.

24. Ashcroft N. and Mermin N., *Solid Sate Physics.*, Saunders College Publishing, **1976**.

25. Morrison S. *The Chemical Physics of Surfaces.*, Plenum Press, New York, **1977**.

26. Gutarra A., *Electrochromism in Titanium Dioxide and Titanium Oxifluoride Thin Films,* PhD Thesis, , National University of Engineering, Lima, **1998**.

27. Claesson S. and Holmström B. *Solar Energy-Photochemical Processes Available for Energy Conversion*, National Swedish Board for Energy Source Development, **1982**.

28. Miller R. J. D., McLendo G. L., Nozik A. J., Schmickler W. and Willing F., *Surface Electron Transfer Processes.*, VCH Publisher, New York, **1995**.

29. Nazeeruddin M., Rodicio K., Humphry-Baker R., Liska P., Vlachopoulos N. and Grätzel M., *J. Am. Chem. Asoc.*, **1993**, 115, 6382.

30. Taqui Khan M. M., Chatterjee D., Hussais A. and Moiz M. A., *J. Photochem. Photobiol. A:Chem.*, **1993**, 76, 97.

31. Ihara M., Tanaka K., Sakaki K. Honma I. and Yamada K., *J. Phys. Chem. B*, **1997**, 101, 5153.

32. Kamat P., *Chemtech*, **1995**, 22.

33. Hagfeldt A. and Grätzel M., *Chem. Rev.*, **1995**, 95, 49.

34. Argazzi R., Bignozzi C., Heimer T., Castellano F. and Meyer G., *Inorg. Chem.* **1994**, 33, 5741.

35. Solbrand A., *Charge Transport in Nanostructured Metal Oxide Thin Film Electrodes*, PhD Thesis, Uppsala University, **1998**.

36. Glocker D. A. and Shanh S. I. (editors) *Handbook of Thin Film Process Technology-Sputtering*, IOP Publ., Bristol, **1995**.

37. Chapman B., *Glow Discharge Processes*, Willey, New York, **1980**.

38. Solis J., *Physical Characterization and Gas-Response Studies of Stannous Tungsate*, PhD Thesis, National University of Engineering, Lima, **1997**.

39. Vossen J. L. and Kern R. (editors) *Thin Film Processes*, Academic, New York, **1978**.

40. Kharrazi M., *High Magnetron Sputter Deposition of Thin Al Oxide and Mo Oxide Films*, Lic. Thesis, Uppsala University, **1997**.

41. Ohring M., *The Materials Science of Thin Films*, Academic, New York, **1992**.

42. LeBellac D., Niklasson G. A. and Graqvist C. G., *J. Appl. Phys.* **1995**,77, 6145.

43. Powder Diffraction Files (Int. Center for Diffraction Data); files 21-1272 and 21-1276.

44. Cullity B. D., *Elements of X-ray Diffraction*, Addison-Wesley, Reading, **1959**.

45. Binning G., Roher H. and Gerber C., *Phys. Rev. Lett.*, **1982**, 49, 57.

46. Binning G., Quate C. F. and Gerber C., *Phys. Rev. Lett.*, **1986**, 56, 930.

47. Wiesendanger R. and Güntherodt (editors) *Scanning Tunneling Microscopy II*, Springer-Verlag, Berlin, **1992**.

48. Reimer L., *Scanning Electron Microscopy: Physics of Image Formation and Microanalysis*, Springer Series in Optical Sciences, Vol 45, Springer-Verlag, Berlin, **1985**.

49. Bard A. J. and Faulkner L. R. *Electrochemical Methods*, John Willey & Sons, New York, **1980**.

50. Skoog D. A. and Leary J. J., *Principles of Instrumental Analysis*, Saunders College Publishing, New York, **1992**.

51. Resmo H., Lindström H., Södergren S., Willstedt A.-K., Solbrand A. Hagfeldt A. and Lindquist S.-E., *J. Electrochem. Soc.*, **1996**, 143, 3173.

52. Strømme, M., Gutarra, A., Niklasson G.A. and Granqvist C.G., *J. Appl. Phys.*, **1996**, 79, 3749.

53. Linquist S.-E.,Finnström B. and Tegner L., *J. Electrochem. Soc.*, **1983**, 130, 351.

54. Ichikawa S. and Doi R., *Thin Solid Films*, **1997**, 292, 130.

55. Lepore G., Langford, C. Víchová J. and Vlcek A., *J. Photochem. Photobiol. A*, **1993**, 75, 67.

56. Nanoscope III Command Reference Manual Version 3.0 (Digital Instruments, Inc., Santa Barbara, **1993**).

57. Dominey R., Lewis T and Wrighton M., *J. Phys. Chem.*, **1983**, 87, 5345.

Paper I

PHOTOELECTROCHEMICAL PROPERTIES OF POLYCRYSTALLINE Ti OXIDE THIN FILMS PREPARED BY SPUTTERING

M. GÓMEZ, J. RODRÍGUEZ, S.-E. LINDQUIST* AND C.G. GRANQVIST

Department of Materials Science, The Ångström Laboratory, Uppsala University, P.O. Box 534, SE-751 21 Uppsala, Sweden

*Department of Physical Chemistry, Uppsala University, P.O. Box 532, SE-751 21 Uppsala, Sweden
Tel.: +46 018 471 1810, Fax.: +46 018 500 131
E-mail.: monica.gomez@angstrom.uu.se

ABSTRACT. Non-stoichiometric polycrystalline Ti oxide thin films were prepared by reactive DC magnetron sputtering of Ti in O_2+Ar onto Indium Tin Oxide (ITO) coated glass. Rutile and anatase phase films were obtained by heating the substrate during the deposition. Incident photon-to-current efficiency (IPCE) was studied as a function of several sputtering parameters such as temperature of the substrate, film thickness, and O_2/Ar gas flow ratio. The IPCE increased as the crystallinity of Ti oxide was systematically varied from amorphous to a mixture of anatase and rutile, and it was also enhanced in films deposited at low O_2/Ar ratios. The photoresponse was measured using a three-electrode set-up with an electrolyte consisting of an aqueous 0.1 M KI solution purged with nitrogen. Action spectra were scanned between 280 and 400 nm in wavelength. The photogenerated current was found to be highly dependent on the composition, thickness, and structure of Ti oxide films.

1. INTRODUCTION

Titanium oxide is a coating material with very interesting properties. It is hard and chemically resistent, transparent in the visible and near infrared ranges, and has a high refractive index; it is useful for several different optical applications. The films can be prepared by many techniques, such as chemical vapor deposition, reactive DC and RF diode or magnetron sputtering, ion-assisted deposition, and sol-gel processes [1]. Among these techniques, reactive DC magnetron sputtering is of special interest since it is an industrial process applicable to large area deposition.

After the demonstration of a photoresponse of Ti oxide [2], many studies have been performed in order to investigate the photocatalytic and solar cell properties of the material. The purpose of the current work is to demostrate the changes in the photoresponse of Ti oxide thin films prepared by DC magnetron sputtering as a result of variations of the parameters for the deposition.

2. FILM DEPOSITION AND CHARACTERIZATION

The films were prepared by reactive DC magnetron sputtering using a system described elsewhere [3]. After evacuation to ~10^{-7} Torr by turbo molecular pumping, sputtering took place in an atmosphere of Ar (99.998%) mixed with O_2 (99.998%). The O_2/Ar gas flow ratio was kept constant at a value Γ during the film deposition, and the sputtering took place in a total gas pressure of 12 mTorr. The targets were 5-cm-diameter plates of Ti (99.9%) positioned 13 cm from a substrate holder. The substrate temperature τ_s was controlled with a resistive heater, and film uniformity was assured by rotating the substrate. The film thickness was determined by surface profilometry using a Tencor Alpha-Step instrument. Substrates were plates of smooth glass precoated with a layer of transparent and conducting ITO (In_2O_3:Sn) having a resistance/square of 14 Ω.

X-ray diffraction (XRD) was carried out on a Siemens D5000 diffractometer with Cu anode and grazing incidence unit suitable for thin films. Data from standards for TiO_2 were used to identify the diffraction peaks [4]. Scherrer's formula [5] was used to estimate the mean grain size. Figure 1 displays XRD data for Ti oxide films deposited at different values of τ_s. The thickness for all of these films was ~220 nm and Γ was 0.05. No distinct peaks from Ti oxide were obtained at τ_s < 100°C. However, an increase of τ_s to 150°C led to the appearence of one peak assigned to an anatase (101) reflection. This peak became more prominent at τ_s = 200°C. No diffraction peaks due to the rutile phase were visible until τ_s = 250°C; a (101) reflection then became visible. Crystallite sizes corresponding to the anatase (101) peak for films deposited at 150, 200, and 250°C were 7, 13, and 18 nm, respectively, and the crystallite size corresponding to the rutile (101) peak was ~15 nm. Similar data have been observed before [6] for Ti oxide films.

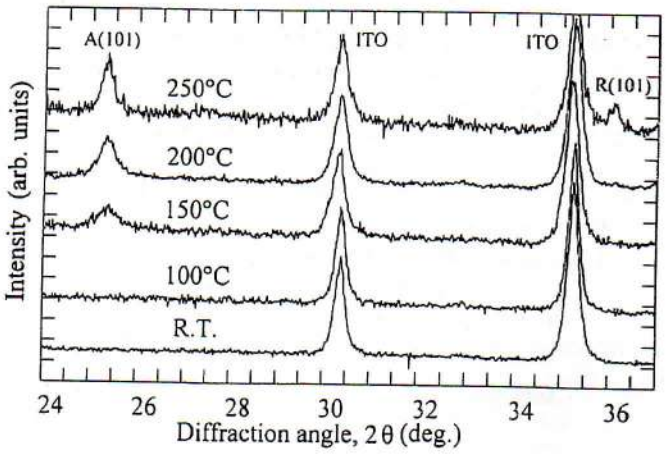

Figure 1. X-ray diffractograms for Ti oxide films on ITO coated glass substrates. The substrate was kept at room temperature (R.T.) and at four elevated temperatures during the sputter deposition. The diffraction peaks are assigned to different reflections in the anatase (A) and rutile (R) structure.

3. INCIDENT PHOTON-TO-CURRENT EFFICIENCY

Incident photon-to-current conversion efficiency (IPCE) was measured in a set-up shown in Fig. 2. The light source was a 450 W Xe lamp whose beam passed through an 80-mm-thick water filter into a high-intensity monochromator (Schoeffel GM 252) and a focusing lens; the beam was then split in two parts by a quartz window, one of the parts (a small fraction) was directed toward a photodiode reading the intensity, and the other part toward the sample. The system was calibrated using an optical power meter (Photodyne Model 44XL) with a silicon photodiode (Model 400 AS) radiometric sensor head. The Ti oxide film was placed as working electrode in a three-electrode system. The counter electrode was a net of Pt enclosed in a glass tube with a frit glass in its extreme end, and the reference was a saturated Calomel electrode. A general-purpose potentiostat (Princeton Applied Research, Model 173) was used for the electrochemical measurements. The electrolyte was 0.1M KI in water purged with nitrogen. The pH was adjusted to 6.6 by a 0.02M potassium phosphate buffer.

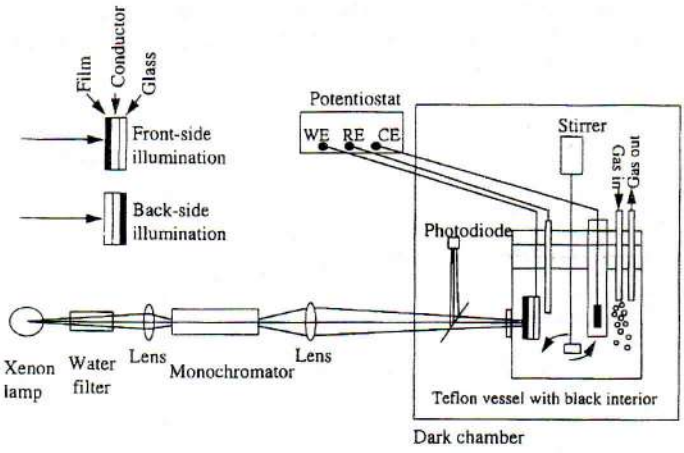

Figure 2. Schematic of the experimental set-up for IPCE measurements.

Action spectra were recorded in the ultraviolet wavelength range, at $280 < \lambda < 400$ nm. At the beginning of each recording session, the working electrode was biased to 0.3 V until it attained a steady state value of the dark current. To prevent systematic errors, the wavelengths at which data were taken were chosen at random. The measurements were corrected for dark currents. IPCE was calculated by

$$\text{IPCE} = 1240 i_{ph}/(P\lambda)\,,$$

where P (in $\mu W/cm^2$) and λ (in nm) are the light power density of the radiation per unit area and the wavelength of the incident monochromatic beam, respectively, and i_{ph} is the photocurrent density (in $\mu A/cm^2$). No corrections were made for absorption and reflection in the substrate.

The following sections illustrate how the IPCE is influenced by different deposition parameters, specifically, the substrate temperature, the O_2/Ar gas flow ratio, and the sputtering time (i.e., the film thickness). Figures 3a and 3b show IPCE data for front-side illumination (light directly onto the film) and back-side illumination (through the conducting glass) for samples deposited at the same temperatures as for the films reported on Fig. 1. The film deposited at τ_s = 250°C reaches a maximum photoresponse of 0.14 at λ = 300 nm. The general trend, common to all samples, is that the quantum efficiency has a maximum value at λ = 300 nm, and that the photoresponse is higher the larger the substrate temperature during film deposition. The action spectra for back-side illumination (Fig. 3b) display a similar correlation between τ_s and IPCE, but distinctive features due to absorption in the glass substrate can be seen for $\lambda <$ 350 nm. Even though the magnitude of the photoresponse is rather low, the striking observation is that a mixture of anatase and rutile phases generates the

best IPCE in our sputter deposited Ti oxide films. This result contrasts with previous reports stating that anatase films are more photoactive than mixed anatase-rutile and pure rutile films [7].

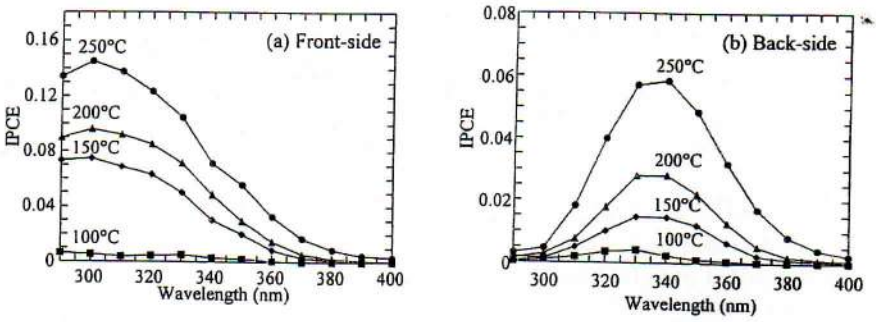

Figure 3. Spectral incident photon-to-current efficiency (IPCE) for front-side (part a) and back-side (part b) illumination of Ti oxide films sputter deposited onto ITO coated glass substrates at the show temperatures.

Considering now the role of the O_2/Ar ratio, Figs. 4a and 4b show IPCE spectra for front-side and back-side illumination of samples deposited at τ_s = 250°C in a total pressure of 12 mTorr. This total pressure was found to give the best photoresponse, at least in the range between 10 and 13 mTorr. The films were about 600 nm thick and the deposition rate was 0.5 nm/s, the only exception being that the film deposited at Γ = 0.078 was ~450 nm thick and was deposited at 0.4 nm/s. The quantum efficiency for front-side illumination of the sample deposited at Γ = 0.069 reaches a maximum of as much as 0.75 at λ = 310 nm. This value is higher than the ones reported before for polycrystalline films [7,8]. Data on front-side illumination onto films deposited at Γ = 0.071 and Γ = 0.073 show the same spectral features as for the film deposited at Γ = 0.069, but the enhanced oxygen admixure produces a systematic decrease in the photoresponse. Films deposited at even higher O_2 contents display the same trend in the spectral photoresponse, but it is noteworthy that the film deposited at Γ = 0.075 yields two peaks in the IPCE at the wavelengths 370 and 310 nm, while the film deposited at Γ = 0.078 shows only one maximum at λ = 340 nm. In the case of back-side illumination, the distinctive spectral features upon increased Γ are a decreased photoresponse and a shift of the maximum IPCE toward shorter wavelengths.

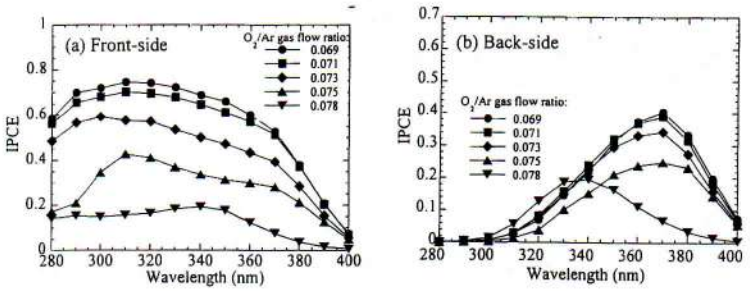

Figure 4. Spectral incident photon-to-current efficiency (IPCE) for front-side (part a) and back-side (part b) illumination of Ti oxide films sputter deposited onto ITO coated glass substrates at the shown O_2/Ar gas flow ratios.

The influence of film thickness is described in Figs. 5a and 5b, showing IPCE spectra for front-side and back-side illumination of samples deposited at τ_s = 250°C for different periods of time in order to obtain a range of thicknesses. The deposition rate and Γ were 0.5 nm/s and 0.074, respectively. Figure 5a gives clear evidence for the importance of having a suitable film thickness. The thinnest film, with a thickness of 279 nm, displays a maximum photoresponse of 0.43 at λ = 300 nm, while the 432-nm-thick film has a maximum photoresponse of 0.67 at the same wavelength. Back-side illumination produces similar trends for the relation between IPCE and film thickness but also shows a shift of the maximum IPCE values towards longer wavelength as the film becomes thicker. Detailed models both for solid [8] and porous [9] thin films have earlier been developed for analysis of action spectra derived from front- and back-side illumination experiments. Data in the present report will in a full paper be subject to such an analysis in a forthcoming paper.

4. SUMMARY

We prepared polycrystalline Ti oxide films on conducting glass substrates by reactive DC magnetron sputtering. The photoresponse was measured using established techniques. A maximum incident photon-to-current efficiency of 0.75 at a wavelength of 310 nm was obtained for films with a suitable stoichiometry (obtained by controling the gas composition in the sputter plasma) and having a thickness of about 0.6 μm. The substrate temperature during film manufacturing was 250°C, which led to a mixed anatase-rutile structure.

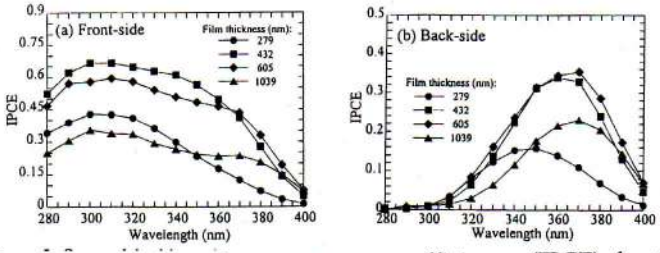

Figure 5. Spectral incident photon-to-current efficiency (IPCE) for front-side (part a) and back-side (part b) illumination of Ti oxide films, having different thicknesses, sputter deposited onto ITO coated glass substrates.

The critical effect of the deposition parameters points at the possibility of achieving still higher magnitudes of the photoresponse. After sensitization of the Ti oxide in a suitable dye, it is possible to extend the spectral range of the photoresponse, as discussed in a separate paper [10], and it hence appears that magnetron sputtering can be developed into a technique for preparation of solar cells of the Grätzel type [11].

Acknowledgment: We appreciate very valuable assistance by Nils-Olov Ersson for the XRD data. Two of us (M.G. and J.R.) want to thank the International Science Programs, Uppsala University, for scholarships.

REFERENCES

[1] Granqvist, C.G. (1995), Handbook of Inorganic Electrochromic Materials, Elsevier, Amsterdam, pp. 266-267.
[2] Fujishima, A. and Honda, K. Nature 238 (1972) 37.
[3] Le Bellac, D., Niklasson, G.A. and Granqvist C.G. J. Appl. Phys. 77 (1995) 6145.
[4] Powder Diffraction Files (Int. Center for Diffraction Data) (1997); files 21-1272 and 21-1276.
[5] Cullity, B. D. (1959), Elements of X-ray Diffraction, Addison-Wesley, Reading.
[6] StrØmme, M., Gutarra, A., Niklasson G.A. and Granqvist C.G. J. Appl. Phys. 79 (1996) 3749.
[7] Ichikawa, S. and Doi, R. Thin Solid Films 292 (1997) 130.
[8] Lindquist, S.-E., Finnström, B. and Tegner, L. J. Electrochem. Soc. 130 (1983) 351.
[9] Södergren, S., Hagfeldt, A., Olsson, J., and Lindquist, S.-E., J. Phys. Chem. 98 (1994) 5552.
[10] Gómez, M., Rodríguez, J., Lindquist, S.-E. and Granqvist, C.G. To be published.
[11] O´Regan, B. and Grätzel, M. Nature 353 (1991) 737.

Paper II

EVIER

Thin Solid Films 342 (1999) 148–152

thin solid films

ıotoelectrochemical studies of dye-sensitized polycrystalline titanium oxide thin films prepared by sputtering

M. Gómez[a], J. Rodríguez[a], S.-E. Lindquist[b], C.G. Granqvist[a,*]

[a]*Department of Materials Science, The Ångström Laboratory, Uppsala University, P.O. Box 534, SE-751 21 Uppsala, Sweden*
[b]*Department of Physical Chemistry, Uppsala University, P.O. Box 532, SE-751 21 Uppsala, Sweden*

Received 1 September 1998; received in revised form 7 October 1998; accepted 7 October 1998

ract

anium oxide thin films were prepared by reactive DC magnetron sputtering of Ti in O_2 + Ar onto SnO_2:F coated glass. A dye consisting s-dithiocyanato-*N*-bis(2,2′-bipyridyl-4,4′-dicarboxylic acid) ruthenium (II) was incorporated by dipping the films into a solution of the n ethanol. The amount of dye incorporation was found to be highly dependent on the microstructure and the thickness of the film, as rent from optical measurements. Incident photon-to-current efficiency was studied as a function of sputtering parameters using a three-rode cell with an electrolyte consisting of an aqueous 0.1 M KI solution purged with nitrogen as well as using a two-electrode system acetonitrile with a LiI/I_2 solution as the electrolyte.

ords: Titanium oxide thin film; Dye sensitization; Polycrystalline; Photoelectrochemistry

ıtroduction

itanium oxide is a semiconductor that holds much nise for photoelectrochemical applications related to rgy conversion [1–3]. The material is of large interest solar cells [4,5] and for photocatalytic destruction of anic pollutants in wastewater [6–8]. Other potential lications concern optical devices [9,10] and electrical eries [11], and the hardness of Ti oxide makes this mate- of importance for protective uses.

he purpose of the present work is to explore the possi-ties to employ sputter-deposited Ti oxide films in solar s. Sputtering as a thin film preparation technique is of ticular significance owing to its well documented upscal- capability and its industrial viability [12]. Some vious work on sputter-deposited Ti-oxide-based solar s has been reported by Sheng et al. [13].

Film preparation and characterization

Oxide films were deposited using reactive DC magnetron ttering in a system based on a Balzers UTT 400 vacuum mber [14]. The targets were 5-cm-diameter metallic tes of Ti (99.9%). The chamber was evacuated to 0^{-7} Torr by turbo molecular pumping. Prior to sputter deposition, Ar (99.998%) and O_2 (99.998%) gas were introduced via separate mass-flow-controlled inlets. The O_2/Ar gas flow ratio was kept constant at a value Γ. The pressure in the sputter plasma was 12 mTorr. The films were deposited onto glass substrates precoated with a layer of transparent and conducting SnO_2:F having a resistance/square of 8 Ω. Film uniformity was assured by rotating the substrate during the deposition. The film thickness d was determined by surface profilometry using a Tencor Alpha-Step instrument. Deposition rate was obtained by dividing d by sputtering time. Typically, the rate was 0.5 nm/s.

Surface morphologies were studied with scanning electron microscopy (SEM) and atomic force microscopy (AFM) using Zeiss DSM 960 and Nanoscope II instruments, respectively. Fig. 1a shows a SEM image of the bare surface of the SnO_2:F coated conducting glass. This surface has a rough appearance with crystalline nodules being around 400 nm in linear extent. Front surfaces of 170-nm-thick and 1040-nm-thick Ti oxide film electrodes, deposited onto the coated substrate, are shown in Fig. 1b,c, respectively. The thinnest film displays the expected replication of the substrate roughness [14]. However, by increasing the thickness of the Ti oxide electrode, it seems to loose its correlation with the underlying SnO_2:F surface, and the SEM image shows a three-dimensional network of interconnected Ti oxide nodules each being around 100 nm in size.

Surface topographies were also analyzed by AFM, and Fig. 2 shows typical micrographs taken for the same type of

Corresponding author. Tel.: +46-18-471-3067; fax: +46-18-500-131.
E-mail address: claes-goran.granqvist@angstrom.uu.se (C.G. Granqvist)

40-6090/99/$ - see front matter
: S0040-6090(98)01482-5

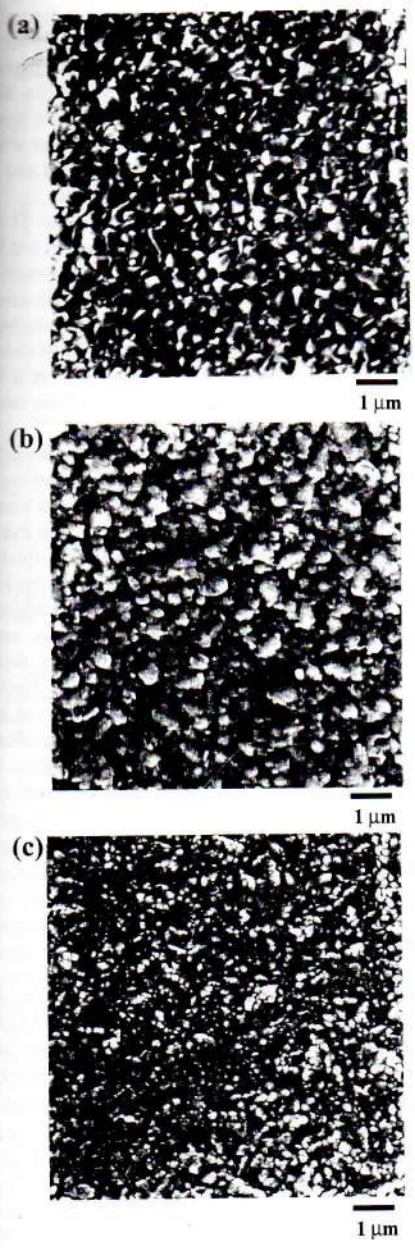

g. 1. (a) SEM image of the bare surface of the SnO_2:F coated conducting ass. Front surfaces of 170-nm-thick (b) and 1040-nm-thick (c) Ti oxide m electrodes deposited onto the coated substrate.

mples as in Fig. 1. Generally, the AFM data show rough-ess that correlates well with the SEM images. The 170-nm-ick electrode illustrated in Fig. 2b seems to comprise

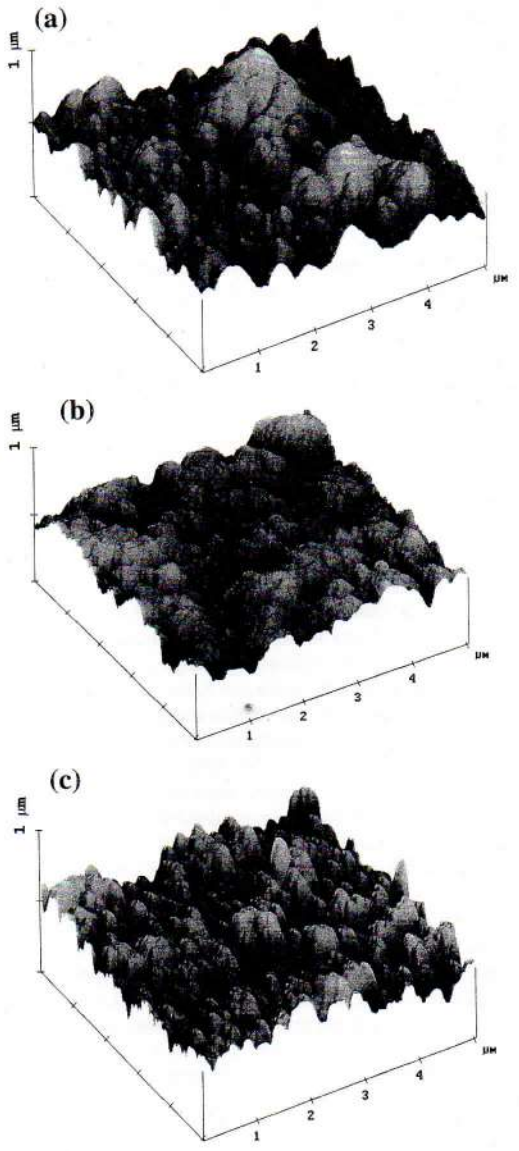

Fig. 2. Typical micrographs taken for the same type of samples as in Fig. 1.

small features that are about 30 nm in size resting on larger ones resulting from the transparent conductor. The horizontal extents of the roughness features are similar for the 170-nm-thick and the 1040-nm-thick Ti oxide films, but an increase of the protrusion height is evident for the thickest film.

Structural studies were made by X-ray diffraction (XRD) using a Siemens D5000 diffractometer with Cu anode and grazing incidence unit. Data from TiO_2 standards [15] were

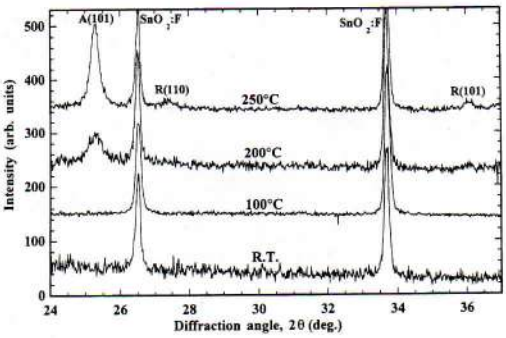

Fig. 3. Grazing incidence X-ray diffractograms for Ti oxide films sputtered onto conducting glass kept at different values of the substrate temperature. The thickness for all of the films is ~260 nm. A and R refer to the anatase and rutile structures, respectively.

used to identify the diffraction peaks. The mean grain size D was estimated from Scherrer's formula, i.e.,

$$D = \frac{K\lambda_x}{\beta\cos\theta} \tag{1}$$

where K is a dimensionless constant, 2θ is the diffraction angle, λ_x is the X-ray wavelength, and β is the full width at half maximum of the diffraction peak.

Fig. 3 shows grazing incidence X-ray diffractograms for Ti oxide films sputtered onto conducting glass kept at different values of the substrate temperature τ_s. The thickness for all of the films is ~ 260 nm. No diffraction peaks due to Ti oxide were visible for samples deposited at room temperature, and similar results were obtained for $\tau_s = 100°C$. By setting the substrate temperature at 200°C, however, one peak corresponding to anatase (101) reflections became apparent at $2\theta = 25.3°$. For $\tau_s = 250°C$, one finds clear XRD evidence in favor of an anatase–rutile mixture. A similar dependence of the crystalline structure for Ti oxide on τ_s has been observed before [16]. Applying Scherrer's formula to the anatase (101) peak for films deposited at $\tau_s = 200°C$, the grain size was found to be about 10 nm. For the film deposited at $\tau_s = 250°C$, the grain size derived from the same anatase peak was ~30 nm, whereas the rutile (110) and (101) peaks corresponded to ~8 nm. These magnitudes of D are in the same range as the microcrystallite dimensions of Ti oxide electrodes earlier prepared from nanoparticles [17]. The XRD values of D are consistent with the surface topographic data ensuing from our SEM and AFM analyses.

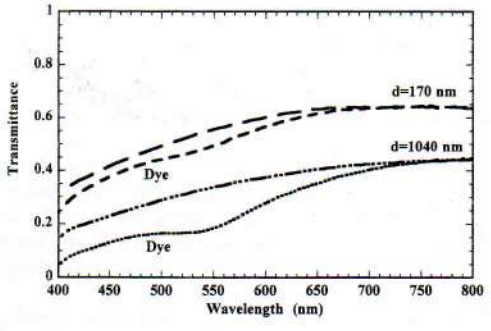

Fig. 4. Transmittance for the 170-nm-thick and the 1040-nm-thick Ti oxide films with and without dye.

Sensitization by adsorption of dye onto the Ti oxide surfaces was carried out by soaking the films in a 0.5 mM solution of Cis-dithiocyanato-*N*-bis(2,2′-bipyridyl-4,4′-dicarboxylic acid) ruthenium (II) in ethanol for one day [21]. The effect of the dye was probed by spectral optical transmittance measurements in the visible wavelength range, i.e. at $400 < \lambda < 800$ nm, using a Perkin-Elmer Lambda 9 double-beam spectrophotometer with an integrating sphere.

Fig. 4 shows the transmittance for the 170-nm-thick and the 1040-nm-thick Ti oxide films with and without dye. The films are strongly light scattering. The maximum transmittance of the 170-nm-thick film (with and without dye) it is around 0.64 at $\lambda = 750$ nm, while the 1040-nm-thick film has a maximum transmittance (in the absence of dye) of no more than 0.44 at the same wavelength. The dye absorption band for the 1040-nm-thick sensitized electrode is centered at 540 nm in wavelength and may be broader than the absorption band apparent in the 170-nm-thick electrode. The data in Fig. 4 give clear evidence in favor of a film thickness dependence of the dye incorporation. Furthermore, the influence from the film roughness seems to be high, and Ti oxide films deposited under the same conditions as those used to obtain Fig. 4 onto very smooth surfaces did not display any absorption due to the dye sensitization.

3. Incident photon-to-current efficiency

Incident photon-to-current efficiency (IPCE) was determined from experiments using three- and two-electrode cells. Spectral data were registered point by point, taking random values of the wavelength to avoid systematic errors during the measurement. The IPCE was then calculated from

$$\mathrm{IPCE} = \frac{1240 i_{ph}}{P\lambda} \tag{2}$$

where i_{ph} (in $\mu A/cm^2$) and P (in $\mu W/cm^2$) are photocurrent and power of the incident radiation per unit area, respectively, and λ (in nm) is the wavelength of the light. No corrections were made for absorption and reflection in the substrate.

Three-electrode measurements on unsensitized samples were performed as described elsewhere [18]. The Ti oxide sample was placed as a working electrode. The counter electrode was a net of platinum enclosed in a glass tube

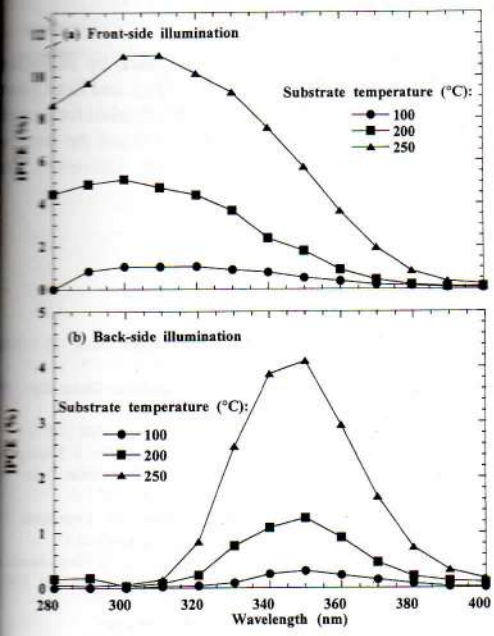

Fig. 5. IPCE data for (a) front-side illumination (light directly onto the film) and (b) back-side illumination (light through the conducting glass) in the three-electrode set-up for films deposited at the same substrate temperatures and having the same thicknesses as for the samples reported in Fig. 3.

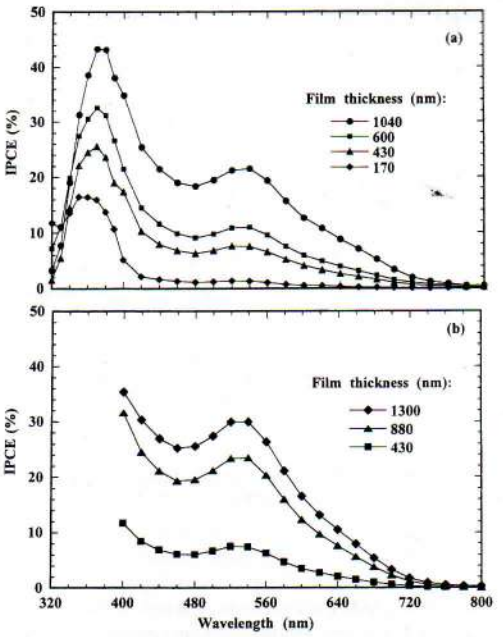

Fig. 6. (a) IPEC data for a series of Ti oxide samples sputter deposited in direct succession so that films with different thicknesses were obtained. The film with $d = 1040$ nm has a maximum IPCE of about 20%, while the thinner films display IPCEs that decrease with diminishing thickness. (b) Results for another series of Ti oxide films analogous to the one in part (a).

with a frit glass in one end, and the reference was a saturated Calomel electrode. A general-purpose potentiostat (Princeton Applied Research, Model 173) was used for the electrochemical measurements. The electrolyte was 0.1 M KI in water purged with nitrogen; it was found to give a stable photoresponse. The pH was adjusted to 6.6 by a 0.02 M potassium phosphate buffer. The potential applied to the working electrode was 0.3 V; this voltage gave the highest photoconversion efficiencies.

Fig. 5a,b shows IPCE data for front-side illumination (light directly onto the film) and back-side illumination (light through the conducting glass) in the three-electrode set-up for films deposited at the same substrate temperatures and having the same thicknesses as for the samples reported in Fig. 3. All spectra were measured only in the ultraviolet range, i.e., at $280 < \lambda < 400$ nm. The action spectra for front-side and back-side illumination of the corresponding Ti oxide electrodes show a number of common features. Specifically, the photoresponse is higher the larger the substrate temperature used for the deposition of the film, and the spectrum for front-side illumination of the film deposited at $\tau_s = 250$°C yields 11% as the maximum photoresponse at $\lambda = 300$ nm, while the maximum value obtained for the film obtained at $\tau_s = 100$°C is only around 1%. The action spectra for the back-side illumination display distinctive features due to the absorption at $\lambda < 350$ nm in the transparent conducting layer. Similar data have been recorded before for polycrystalline films [19]. Even though the magnitude of the IPCE is rather low, the striking and novel observation in Fig. 5 is that a mixture of the anatase and rutile phases generates the best photoresponse in our sputter deposited Ti oxide films. The crystal size and porosity presumably are important as well; their specific influence remains to be investigated.

Two-electrode measurements were performed with dye-sensitized Ti oxide films pressed together with a Pt foil using a spring. The electrolyte was 0.5 M LiI/0.05 M I_2 in acetonitrile. A two-electrode solar cell set-up was used to measure IPCE spectra in the ultraviolet and visible wavelength ranges for different thickness of Ti oxide electrodes. Data are reported in Fig. 6, where part a refers to one series of Ti oxide samples sputter deposited in direct succession so that films with different thicknesses were obtained. The film with $d = 1040$ nm has a maximum IPCE of about 20%, while the thinner films display IPCEs that decrease with diminishing thickness. Fig. 6b contains results for another series of Ti oxide films analogous to the one reported on in Fig. 6a. By comparing the two sets of data, it is possible to verify the reproducibility of the photoresponse with the change of film thickness. Furthermore, it is found that the 1300-nm-thick Ti oxide film in Fig. 6b has a maximum

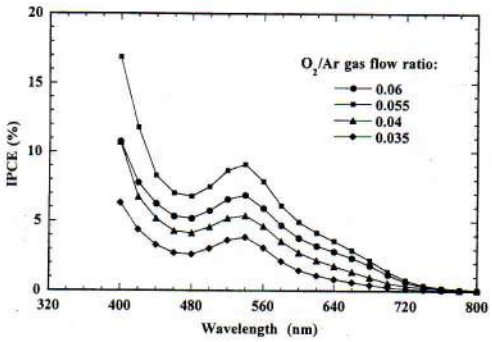

Fig. 7. Results from a series of Ti oxide films deposited at different values of the O_2/Ar gas flow ratio. The rest of the parameters for the sputtering deposition were kept constant.

IPCE of about 30%, which is comparable to data for films prepared from nanoparticles [20].

Fig. 7 gives unambiguous evidence for the importance of having suitable film preparation conditions by showing results from a series of Ti oxide films deposited at different values of the O_2/Ar gas flow ratio. The rest of the parameters for the sputtering deposition were kept constant. All of these films were about 500 nm thick and were deposited at $\tau_s = 250$°C. The film deposited at $\Gamma = 0.06$ shows a peak in the IPCE at $\lambda = 540$ nm equal to 7%. Decreasing Γ to 0.055 makes the peak in the IPCE rise to 9%, while lowing Γ still further makes the IPCE go down strongly. Clearly the composition of the sputtering plasma strongly affects the properties of the films and has a significant influence on the incident photon-to-current efficiency. However the details are not understood.

4. Conclusions

Polycrystalline sputter deposited Ti oxide thin film electrodes having mixed anatase–rutile structure had higher incident photon-to-current efficiency than amorphous and fine-grained anatase phase electrodes. Thick dye-sensitized semiconductor films showed a photoresponse as high as 30% at a wavelength of 530 nm. The incident photon-to-current efficiency depends strongly on the morphological and structural properties of the electrodes, and optimization appears possible by properly tuning the deposition conditions.

Acknowledgements

We appreciate very valuable assistance by Nils-Olov Ersson for the XRD data, Richard Karmhag, and Eva Olsson for the SEM measurements. José Solís is thanked for providing AFM images. M.G. and J.R. want to thank the International Science Programs at Uppsala University for scholarships.

References

[1] K. Rajeshwar, P. Singh, J. DuBow, Electrochim. Acta 23 (1978) 1117.
[2] M. Hoffmann, S. Martin, W. Choi, D. Bahnemann, Chem. Rev. 95 (1995) 69.
[3] A. Mills, S. Le Hunte, J. Photochem. Photobiol. A 108 (1997) 1.
[4] A. Hagfeldt, B. Didriksson, T. Palmqvist, H. Lindström, S. Södergren, H. Rensmo, S.-E. Lindquist, Solar Energy Mater. Solar Cells 31 (1994) 481.
[5] C. Barbé, F. Arendse, P. Comte, M. Jirousek, F. Lenzmann, V. Shklover, M. Grätzel, J. Am. Ceram. Soc. 80 (1997) 3157.
[6] R. Matthews, in: E. Pellizzetti, M. Schivello (Eds.), Photochemical Conversion and Storage of Solar Energy, Kluwer, Dordrecht, 1991, pp. 427.
[7] K. Vinodgopal, P. Kamat, Chemtech. 26 (1996) 18.
[8] L. Su, Z. Lu, J. Photochem. Photobiol. A 107 (1997) 245.
[9] S. Nandra, J. Vac. Sci. Technol. A 8 (1990) 3179.
[10] A. Gutarra, A. Azens, B. Stjerna, C.G. Granqvist, Appl. Phys. Lett. 64 (1994) 1604.
[11] Y. Yagi, M. Hibino, T. Kudo, J. Electrochem. Soc. 144 (1997) 4208.
[12] K. Wasa, S. Hayakawa, Handbook of Sputter Deposition Technology, Noyes, Park Ridge, NJ, 1992 p. 1.
[13] J. Sheng, J. Karasawa, T. Fukami, J. Mater. Sci. Lett. 16 (1997,) 1709.
[14] D. Le Bellac, G.A. Niklasson, C.G. Granqvist, J. Appl. Phys. 77 (1995) 6145.
[15] D. Rönnow, J. Isidorsson, G.A. Niklasson, Phys. Rev. E 54 (1996) 4021.
[16] Powder Diffraction Files (Int. Center for Diffraction Data); files 21-1272 and 21-1276.
[17] M. Strømme, A. Gutarra, G.A. Niklasson, C.G. Granqvist, J. Appl. Phys. 79 (1996) 3749.
[18] G. Lepore, C. Langford, J. Víchová, A. Vlcek, J. Photochem. Photobiol. A 75 (1993) 67.
[19] H. Rensmo, H. Lindström, S. Södergren, A.-K. Willstedt, A. Solbrand, A.A. Hagfeldt, S.-E. Lindquist, J. Electrochem. Soc. 143 (1996) 3173.
[20] S.-E. Lindquist, B. Finnström, L. Tegner, J. Electrochem. Soc. 130 (1983) 351.
[21] H. Lindström, H. Rensmo, S. Södergren, A. Solbrand, S.-E. Lindquist, J. Phys. Chem. 100 (1996) 3084.

Paper III

ELSEVIER

Solar Energy Materials & Solar Cells 59 (1999) 277–287

Solar Energy Materials & Solar Cells

www.elsevier.com/locate/solmat

Photoelectrochemical effect in dye sensitized, sputter deposited Ti oxide films: The role of thickness-dependent roughness and porosity

M. Gómez[a], J. Rodríguez[a], S. Tingry[b], A. Hagfeldt[c], S.-E. Lindquist[c], C.G. Granqvist[a,*]

[a]*Department of Materials Science, The Ångström Laboratory, Uppsala University, P.O. Box 534, SE-751 21 Uppsala, Sweden*

[b]*Laboratoire d'Electrochimie Organique et de Photochimie Redox, Université Joseph Fourier de Grenoble, UMR CNRS 5630 B.P. 53, F- 38401 Grenoble Cedex 9, France*

[c]*Department of Physical Chemistry, Uppsala University, P.O. Box 532, SE-751 21 Uppsala, Sweden*

Received 7 January 1999; received in revised form 22 March 1999

Abstract

Ti oxide films were made by reactive DC magnetron sputtering onto electrically conducting glass substrates. The films were dye sensitized with an Ru complex, thereby yielding nanocrystalline solar cells. We investigated the microstructure of the films by X-ray diffraction, scanning electron microscopy, atomic force microscopy, and cyclic voltammetry on viologen-containing samples. The internal surface area was enhanced with increasing film thickness, and this property could be correlated with an enlarged photoelectric conversion efficiency. © 1999 Elsevier Science B.V. All rights reserved.

Keywords: Thin films; Ti oxide; Solar cells; Photoelectric effects; Sputtering; Electrochemistry

1. Introduction

Nanocrystalline dye-sensitized Ti oxide films have been extensively studied for use as photoelectrodes, especially in solar cells [1–3]. It is generally known that the

* Corresponding author. Department of Materials Science, The Ångström Laboratory, Uppsala University, P.O. Box 534, SE-751 21 Uppsala, Sweden.

PII: S0927-0248(99)00044-6

light-driven electrochemical processes are regenerative, and that the working voltage produced by the device is the difference between the chemical potential of the Ti oxide and the redox potential of a mediator (normally I^-/I_3^-). The details of the physics and chemistry are debated, and much work is currently devoted to investigating issues such as complex multistep surface reactions [4–6], charge recombination [7], and instabilities [8].

The present work is a follow-up on our previous observation [9] that sputter-deposited Ti oxide films can be used in solar cells. Specifically, we investigate the effect on the photoelectric conversion efficiency of the thickness dependent microstructure, as determined by X-ray diffraction, scanning electron microscopy, atomic force microscopy and by cyclic voltammetry on viologen-containing samples [10]. Sputtering is an interesting thin-film deposition technique which is industrially viable and has proven upscaling capability [11,12]. Deposition rates up to 0.4 nm/s have been reported [13].

2. Film preparation

Films were made by reactive DC magnetron sputtering using a system based on a Balzers UTT 400 vacuum chamber [14]. The targets were 5-cm-diameter metallic plates of Ti. The sputtering took place in an atmosphere of Ar (99.998%) and O_2 (99.998%). The O_2/Ar gas flow ratio, determined by mass-flow controlled regulators, was maintained at 0.052, and the total sputter gas pressure was ~ 12.6 mTorr. The target current was kept fixed at 990 mA. Films were deposited onto Libbey Owens Ford glass substrates precoated with a rough layer of electrically conducting SnO_2 : F, having a resistance/square of 8 Ω. Film uniformity was assured by rotating the substrate during the deposition.

The film thickness d was determined by surface profilometry using a Tencor Alpha-Step instrument. Film thicknesses lay in the $1.9 < d < 8.0$ μm range. The deposition rate was obtained by dividing d by sputtering time. Typically, the rate was as large as ~ 0.4 nm/s. The substrate temperature was held constant at 250°C in order to obtain a polycrystalline anatase-rutile structure, which is known to provide a higher photoresponse than an amorphous Ti oxide film [9].

3. Film characterization

The thickness-dependent microstructure of the Ti oxide films is of critical importance for their photoelectrical conversion efficiency. The microstructure was investigated by four different techniques that are able to yield complementary information, viz. X-ray Diffractometry (XRD), Scanning Electron Microscopy (SEM), Atomic Force Microscopy (AFM), and Cyclic Voltammetry (CV) on Ti oxide electrodes incorporating viologen.

3.1. X-ray diffractometry

Structural characterization of the Ti oxide films was performed by XRD, using a Siemens D5000 diffractometer operating with Cu K_α radiation in a conventional θ–2θ set-up. Fig. 1 shows data for films with $1.9 < d < 8$ μm. At 1.9, 6.7 and 8 μm, the diffractograms display two prominent peaks due to the rutile (1 1 0) and (1 0 1) reflections, as well as a small peak assigned to anatase (101) [15]. The film with $d \approx 4.2$ μm displayed an unexpectedly strong anatase peak. The different crystalline structures may be associated with the fact that the film with $d = 4.2$ μm was deposited at 0.3 nm/s, whereas the other films were made with a deposition rate of 0.42 nm/s. Diffraction features due to SnO_2 : F were visible in all cases.

Scherrer's equation [16] was applied to the rutile (1 0 1) peaks for all of the samples in order to assess the mean crystal size. It was found to vary monotonically with film thickness and, somewhat unexpectedly, the thickest films had the smallest grain size. Specifically, the films whose thicknesses were 1.9 and 8 μm had mean grain sizes of 25 and 18 nm, respectively.

3.2. Scanning electron microscopy

Surface morphologies were studied with SEM using a Zeiss DSM 960 instrument operated at 20 kV. Fig. 2a displays the surface of the SnO_2 : F coated electrically conducting glass substrate, which is found to be rough on the scale of 0.4 μm. Fig. 2b-e show SEM images of the surfaces for four samples with different film thicknesses, deposited onto the SnO_2 : F coated glass. Rough surfaces with well-rounded protruding nodules are apparent. The nodular size grows with increasing film thickness from ~ 0.2 μm at $d \approx 1.9$ μm to ~ 0.5 μm at $d \approx 8$ μm. It is apparent that the roughness of the Ti oxide film does not directly mirror that of the underlying substrate.

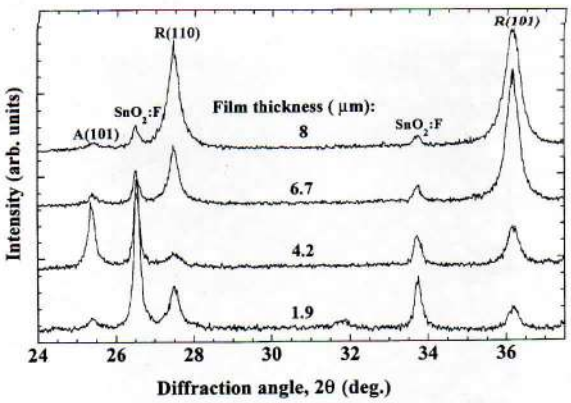

Fig. 1. X-ray diffractograms for Ti oxide films on glass substrates precoated with SnO_2 : F. Data are given for different film thicknesses. The diffraction peaks are assigned to the shown reflections in the anatase (A) and rutile (R) structure in Ti oxide. Additional peaks originate from SnO_2 : F.

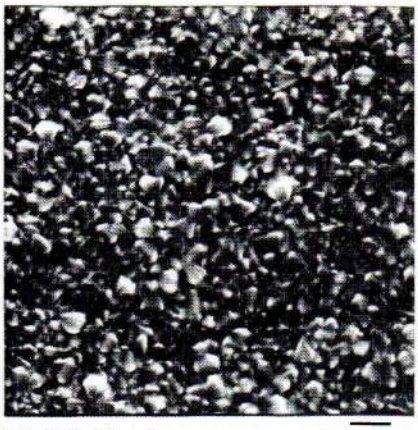

(a) SnO_2:F surface 1 μm

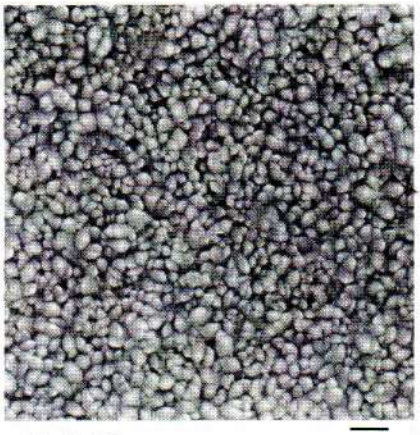

(b) $d = 1.9$ μm 1 μm

(c) $d = 4.2$ μm 1 μm

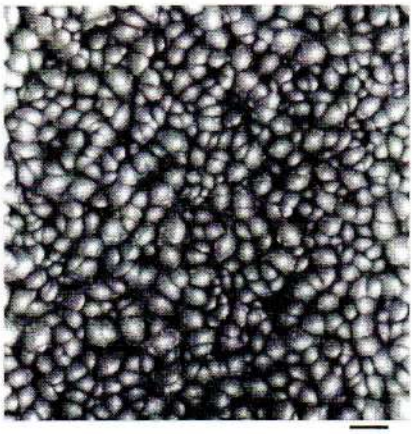

(d) $d = 6.7$ μm 1 μm

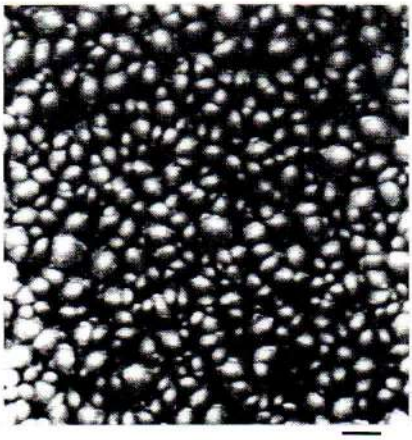

(e) $d = 8.0$ μm 1 μm

3.3. Atomic force microscopy

AFM measurements were made using a NanoScope III instrument with an etched silicon cantilever. Data were taken in ambient air with a contact force of about 10^{-7} N. Scans were extended over areas of 2×2 μm. Fig. 3 shows AFM images. The surface structure is represented by domains, that are about 0.25 μm in diameter for the 1.9 μm thickness film and increase to 0.4 μm for the 8 μm film. The root mean square (RMS) roughness R_{AFM} is defined by

$$R_{AFM} = \left[\frac{\sum_{n=1}^{N} \sum_{m=1}^{M} z_{nm}^2}{NM} \right]^{1/2}, \quad (1)$$

where z_{nm} is the height difference from the average height level for the point whose coordinates are given by the numbers n and m. The data on R_{AFM} were obtained by employing software supplied with the instrument [17]. The roughness grows larger in the thicker films, as seen from Fig. 4. Specifically, the film with $d = 1.9$ μm has $R_{AFM} = 49$ nm and the film with $d = 8$ μm has $R_{AFM} = 91$ nm. The increment of the R_{AFM} is associated principally to the increment of the domain size.

3.4. Cyclic voltammetry

Cyclic voltammograms were recorded to obtain data on film porosity by studying the effect of adsorbed viologen molecules on the Ti oxide and considering an electroreactive-nerstian reaction [10]. The Ti oxide film was sensitized with the viologen N(phosphoro-3-propyl),N′-methyl-4,4′-bipyridinium dibromide by soaking the film in a 1×10^{-5} M solution in ethanol. Prior to the sensitization, the Ti oxide film was kept in air at 350°C for 5 min. Then it was dipped into the viologen solution while it was still warm (80°C), and the film was kept immersed for one day.

A roughness factor ρ_{CV}, defined as the ratio between the electrochemically active area and the geometric area, was obtained from cyclic voltammetry measurements in a three-electrode electrochemical cell arrangement connected to a multichannel ECO Chemie Autolab/GPES electrochemical interface. The working electrode was the Ti oxide film sensitized with viologen, the counter electrode consisted of glassy carbon, and the reference electrode was Ag/AgCl in saturated LiCl in anhydrous acetonitrile. The electrolyte was tetrabutylammonium tetrafluoroborate in acetonitrile. All electrochemical measurements were performed under dry conditions in a glovebox containing Ar.

Fig. 5 displays cyclic voltammograms taken at a voltage sweep rate of 10 mV/s for samples with different film thicknesses. The lower peak (at -0.82 V) represents the first reduction peak of the viologen, and the upper peak (at -0.72 V) is the reoxidation wave of the reduced viologen.

Fig. 2. Scanning electron micrographs of an SnO_2 : F coated substrate (a) and of Ti oxide films having the shown values of the thickness d (b–e).

Integration of CV curves such as those in Fig. 5 gave a maximum charge Q for reducing (or oxidizing) the viologen. Then the surface concentration Γ was calculated from

$$\Gamma = \frac{Q}{FpA}, \tag{2}$$

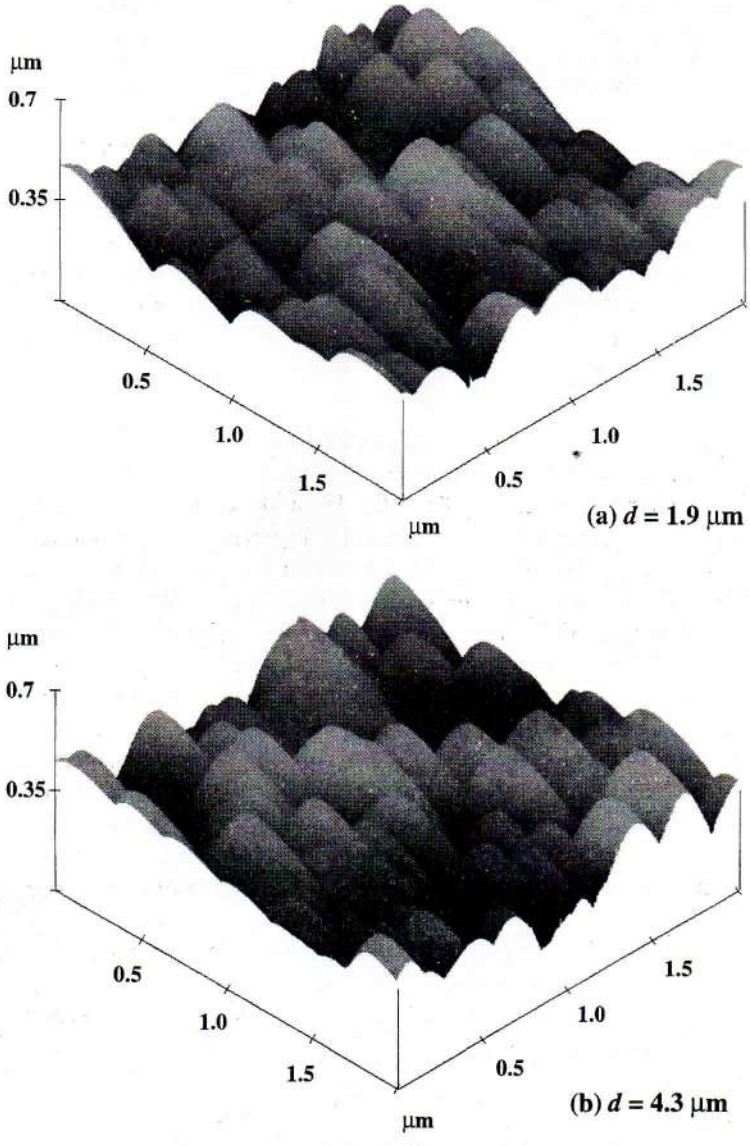

Fig. 3. Atomic force micrographs taken on Ti oxide films having the shown values of the thickness d (a–d).

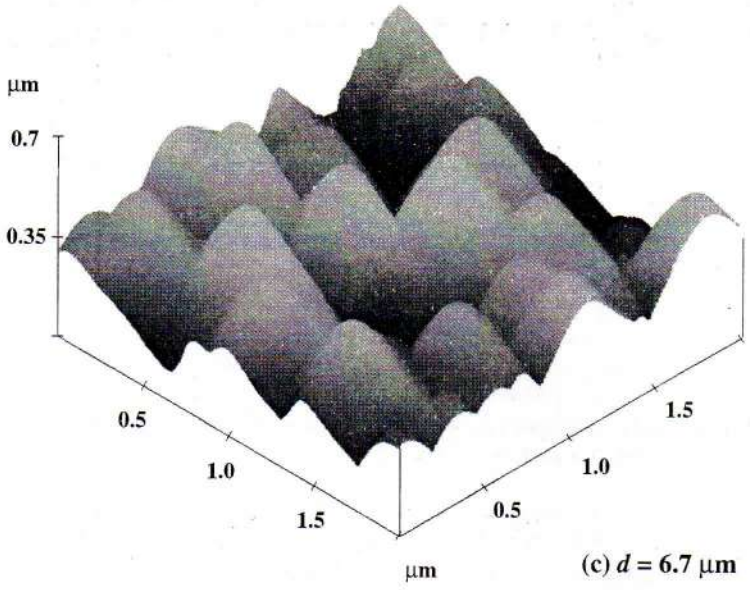

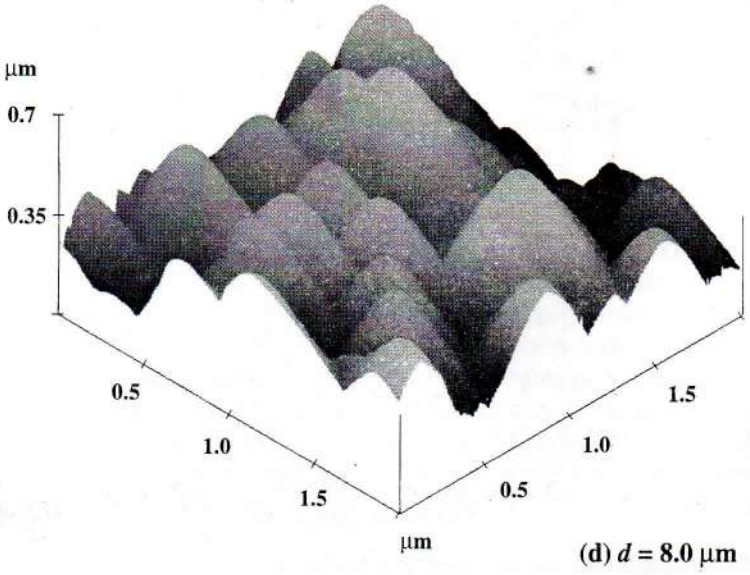

Fig. 3. Continued.

where F is Faraday's constant, p is the number of electrons exchanged during the redox reaction, and A is the area of the electrode. The present conditions correspond to $p = 1$. The roughness factor can be obtained from

$$\rho_{CV} = \frac{\Gamma}{C}, \tag{3}$$

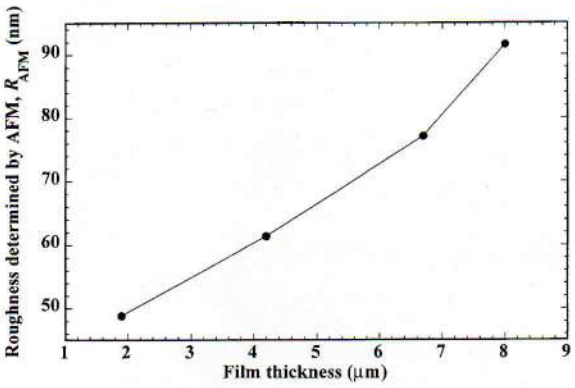

Fig. 4. RMS roughness as determined from AFM for Ti oxide films of different thicknesses. Dots represent data and lines were drawn as a guide to the eye.

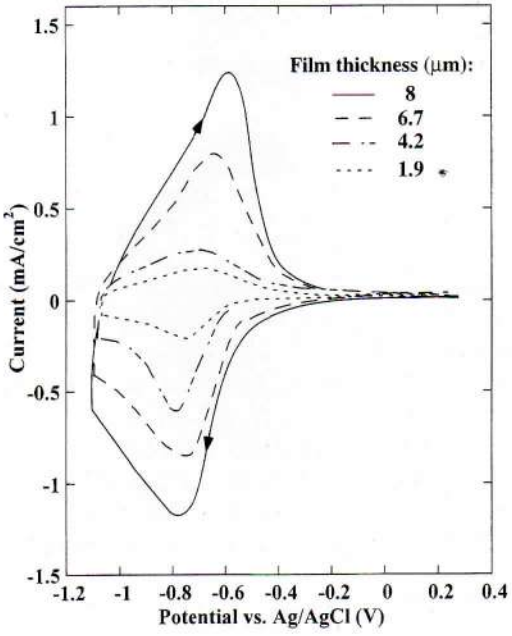

Fig. 5. Cyclic voltammograms for viologen-containing Ti oxide films with different thicknesses. The voltage sweep rate was 10 mv/s. Arrows denote sweep direction.

where C is the fraction of the surface covered by the viologen molecules. An empirical value of C is obtained from the fact that a coverage of $\sim 10^{-10}$ mol/cm^2 corresponds approximately to one monolayer [18]. Evaluations of ρ_{CV} by this procedure yielded the quantities illustrated in Fig. 6. Clearly the roughness factor increases with film thickness in a way that mirrors the CV data in Fig. 5.

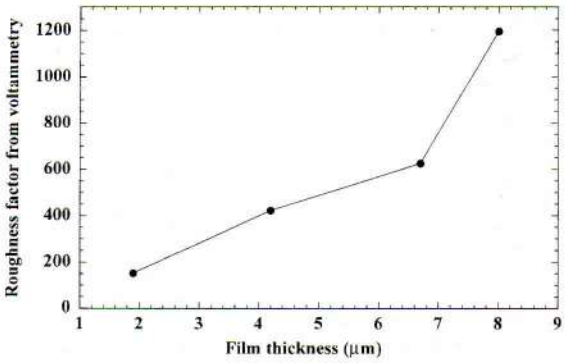

Fig. 6. Roughness factor based on cyclic voltammetry for Ti oxide films with different thicknesses. Dots represent data and lines were drawn as a guide to the eye.

4. Photoelectrical response

The incident photon-to-current efficiency (IPCE) [19] was measured on dye-sensitized Ti oxide films. The sensitization was made with a 5×10^{-4} M solution of cis-dithiocyanato-bis(2,2′-bipyridyl-4,4′-dicarboxylate)-ruthenium (II) in ethanol, i.e. the dye which has shown the best efficiency in earlier work [19,20]. The dye was bought from Solaronix S.A, Switzerland. The dye-coating procedure was the same as for viologen incorporation (Section 3.4). Excess dye was removed by subsequent rinsing with ethanol.

IPCE data were determined using a two-electrode electrochemical sandwich cell in which the dye-sensitized Ti oxide film was squeezed together with a Pt foil using a spring. The electrolyte was 0.5 M LiI/0.05 M I_2 in acetonitrile. The IPCE for the electrodes was measured in the short-circuit mode for substrate/electrode illumination (light incident through the conducting glass). Action spectra were recorded in the visible wavelength range ($400 < \lambda < 800$ nm) using a monochromator of type Schoeffel GM 252. To prevent systematic errors, the wavelengths at which data were taken were chosen at random. No long-term stability tests were made, and corrections for the absorption and reflection in the substrate were not introduced. The light source was a 450 W Xe lamp, and the system was calibrated using an optical power meter (Photodyne Model 44XL) with a silicon photodiode (Model 400 AS) radiometric sensor head.

Fig. 7 shows spectral action spectra for films having the same thicknesses as for the samples reported on in the earlier figures. The data for all of the samples display similar features and, in general, the IPCE rises with increasing film thickness. The data consistently display a peak centered at ~ 530 nm; the feature becomes less distinct in the thicker films.

Fig. 8 illustrates IPCE data for $\lambda = 530$ nm. The photoelectric efficiency improves rather linearly with growing thickness, although some saturation may be apparent in the thickest films.

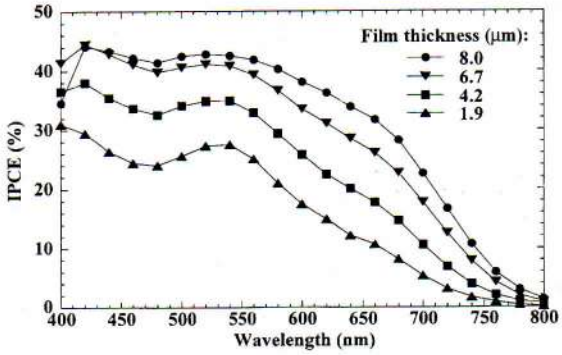

Fig. 7. Spectral incident photon-to-current efficiency (IPCE) for Ti oxide films with the shown thicknesses. Experimental conditions are given in the text. Dots represent data and lines were drawn as a guide to the eye.

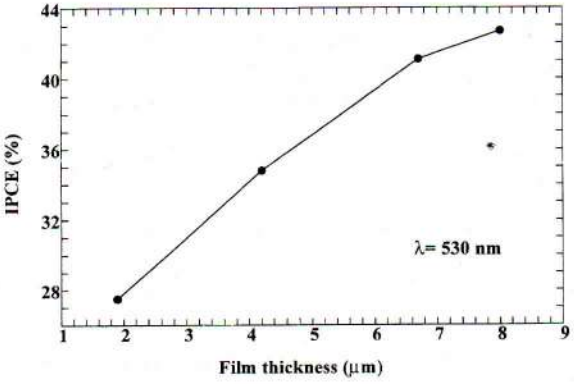

Fig. 8. Incident photon-to-current efficiency (IPCE) at a wavelength of 530 nm for Ti oxide films with different thicknesses. Experimental conditions are given in the text. Dots represent data and lines were drawn as a guide to the eye.

5. Summary and concluding remarks

We prepared Ti oxide films by reactive DC magnetron sputtering and demonstrated that such films can be employed in dye-sensitized nanocrystalline solar cells. The photoelectric conversion efficiency improved monotonically with increasing film thickness, although some saturation may be apparent for thicknesses exceeding $\sim 7\ \mu m$. The microstructures of the films were investigated by several different physical and electrochemical techniques. Generally, the internal surface area increased in the thicker films. The solar cells prepared by sputtering cannot yet compete in efficiency with those made by the more conventional colloidal methods [2,20], but the ability to control the sputtering to achieve different microstructures, and the

proven industrial viability of magnetron sputtering, makes our approach of considerable interest for further studies. Such work is currently in progress.

Acknowledgements

We appreciate very valuable assistance by Richard Westergård for the SEM measurements and by Jesper Ederth and Anders Hoel for the AFM measurements. Two of us (M.G. and J.R.) acknowledge the International Science Programme at Uppsala University for scholarships. S.T. acknowledges the EU-TMR programe (CT 0076) for a post-doctoral stipend.

References

[1] S.-N. Chen, S.K. Deb, H. Witzke, U.S. Patent 4,080,488, 1978.
[2] B. O'Regan, M. Grätzel, Nature 353 (1991) 737.
[3] T. Kasuga, M. Hiramatsu, M. Hirano, A. Hosono, J. Mater. Res. 12 (1997) 607.
[4] A. Hagfeldt, U. Björkstén, S.-E. Lindquist, Solar Energy Mater. Solar Cells 27 (1992) 293.
[5] S. Södergren, A. Hagfeldt, J. Olsson, S.-E. Lindquist, J. Phys. Chem. 98 (1994) 5552.
[6] M. Grätzel, Renewable Energy 5 (1994) 118.
[7] S. Huang, G. Schlichthörl, A. Nozik, M. Grätzel, A. Frank, J. Phys. Chem. B 101 (1997) 2576.
[8] R. Grünwald, H. Tributsch, J. Phys. Chem. B 101 (1997) 2564.
[9] M. Gómez, J. Rodríguez, S.-E. Lindquist, C.G. Granqvist, Thin Solid Films 342 (1999) 148.
[10] A. Bard, L. Faulkner, Electrochemical Methods: Fundamentals and Applications, Wiley, New York, 1980, pp. 521–522.
[11] K. Wasa, S. Hayakawa, Handbook of Sputter Deposition Technology, Noyes, Park Ridge, 1992, pp. 6–9.
[12] W.D. Westwood, in: D.A. Glocker, S.I. Shan (Eds.), Handbook of Thin Film Process Technology, IOP Publ, Bristol, 1998, pp. A5.0.1–A5.0.9.
[13] S. Nandra, J. Vac. Sci. Technol. A 8 (1990) 3179.
[14] D. Le Bellac, G.A. Niklasson, C.G. Granqvist, J. Appl. Phys. 77 (1995) 6145.
[15] Powder Diffraction Files (Int. Center for Diffraction Data); files 21-1272 and 21-1276.
[16] B.D. Cullity, in: Elements of X-ray Diffraction, Addison-Wesley, Reading, MA, 1959.
[17] Nanoscope III Command Reference Manual Version 3.0, Digital Instruments, Inc., Santa Barbara, 1993.
[18] R. Dominey, T. Lewis, M. Wrighton, J. Phys. Chem. 87 (1983) 5345.
[19] M. Nazeeruddin, P. Liska, J. Moser, N. Vlachopoulos, M. Grätzel, Helv. Chim. Acta 73 (1990) 1788.
[20] A. Hagfeldt, M. Grätzel, Chem. Rev. 95 (1995) 49.